Homogenization in Hydrodynamic Lubrication: Microscopic Regimes and Re-Entrant Textures

İ. N. Yıldıran
Department of Mechanical Engineering,
Bilkent University,
Ankara 06800, Turkey

İ. Temizer[1]
Department of Mechanical Engineering,
Bilkent University,
Ankara 06800, Turkey
e-mail: temizer@bilkent.edu.tr

B. Çetin
Department of Mechanical Engineering,
Bilkent University,
Ankara 06800, Turkey

*The form of the Reynolds-type equation which governs the macroscopic mechanics of hydrodynamic lubrication interfaces with a microscopic texture is well-accepted. The central role of the ratio of the mean film thickness to the texture period in determining the flow factor tensors that appear in this equation had been highlighted in a pioneering theoretical study through a rigorous two-scale derivation (Bayada and Chambat, 1988, "New Models in the Theory of the Hydrodynamic Lubrication of Rough Surfaces," ASME J. Tribol., **110**, pp. 402–407). However, the resulting homogenization theory still remains to be numerically investigated. For this purpose, after a comprehensive review of the literature, three microscopic regimes of lubrication will be outlined, and the transition between these three regimes for different texture types will be extensively demonstrated. In addition to conventional textures, representative re-entrant textures will also be addressed.* [DOI: 10.1115/1.4036770]

Keywords: homogenization, hydrodynamic lubrication, Reynolds equation, Stokes equations

1 Introduction

1.1 Multiscale Interface Problem. The pressure that is generated due to the relative motion of two surfaces in close proximity when the interface between them is occupied by a fluid is responsible for the hydrodynamic lubrication effect. The variation of this pressure can be accurately predicted by the Reynolds equation that is formulated with respect to the intrinsically two-dimensional geometry of the interface [1,2], the central geometrical information being the local thickness of the fluid film and the primary solution variable being the pressure—see also Ref. [3] for a recent generalization. The original derivation of the Reynolds equation from Navier–Stokes equations assumes smooth surfaces, i.e., rapid local (microscopic) variations in the film thickness as the global (macroscopic) interface geometry is traversed are omitted from the outset, which leads to an isotropic interface response with respect to pressure gradients and surface velocities. Such microscopic variations naturally occur with surface roughness, leading to a multiscale interface problem (Fig. 1). It is now generally accepted that this multiscale problem will again be governed by a Reynolds-type equation which is still two-dimensional but, due to roughness effects, contains additional terms and is generally anisotropic. It is also established that these differences can be linked with the microscopic effects in a quantitative manner. The formulation of the relevant microscopically informed macroscopic boundary value problem, i.e., a complete *two-scale* formulation, has been a central challenge in lubrication. Many key problems in this challenge have been resolved, and the homogenization theory based on asymptotic expansion, pioneered by Sanchez-Palencia [4], has emerged as a rigorous approach to the formulation of the two-scale problem. However, with recent advances in surface texturing technologies which can construct geometrically complex features in a highly controllable fashion over larger scales and at finer sizes than ever before, the interest in a proper capturing of microscopic effects has been renewed. The investigation of microscopic effects on the macroscopic lubrication response of conventional and representative modern re-entrant textures based on homogenization constitutes the central goal of the present study. For this purpose, the previous work that forms a basis for this investigation will first be reviewed extensively. This review will assume and concentrate on multiscale modeling based on an incompressible flow with a constant viscosity and will omit effects associated with cavitation as well as dissipative heating. The interested reader is referred to the cited works for relevant references which concentrate on such effects.

1.2 Limits of Homogenization. In order to guide the upcoming discussions, it is useful to introduce a number of representative geometrical parameters (Fig. 1). Specifically, L will represent a macroscopic dimension, for instance indicating the size of the lubricated interface, and λ will represent the maximum wavelength associated with the local variations in the film thickness along one or both of the surface coordinates, with an amplitude a. The local average value of the film thickness will be denoted by h_0. One may then define three key dimensionless parameters

$$\eta = h_0/L \ll 1, \quad \varepsilon = \lambda/L \ll 1, \quad \zeta = a/h_0 = \mathcal{O}(0.5) \tag{1.1}$$

The first inequality in Eq. (1.1) is essentially required if a two-dimensional Reynolds-type equation is supposed to govern the macroscopic physics at the interface. For a microscopically smooth interface, this condition is explicitly enforced in the derivation of the Reynolds equation—see Ref. [1] for a traditional dimensional analysis based on Navier–Stokes equations and Ref. [5] for a mathematical analysis in the context of an asymptotic expansion approach applied to Stokes equations. Here, it is important to highlight that in either type of approach η does not physically go to zero but is only employed to extract the limit

[1]Corresponding author.

Contributed by the Tribology Division of ASME for publication in the JOURNAL OF TRIBOLOGY. Manuscript received November 17, 2016; final manuscript received May 11, 2017; published online July 21, 2017. Assoc. Editor: Stephen Boedo.

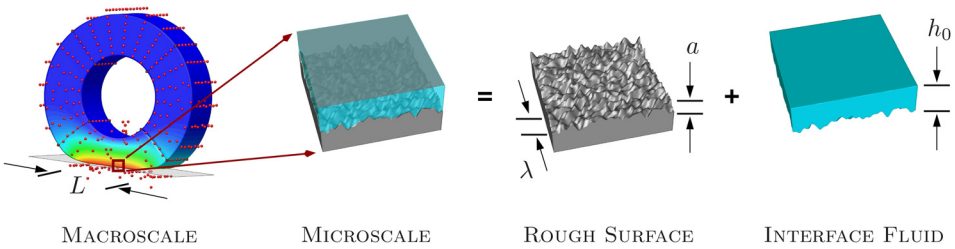

Fig. 1 The multiscale interface problem is depicted, where the numerical solution of the macroscopic problem requires the consideration of the microscale. Here, among representative quantities, *L* is a macroscopic dimension, λ is the wavelength for film thickness variations, h_0 is the local average film thickness, and *a* is the amplitude of the oscillations.

trend in the pressure variation, as for homogenization in porous media [4,6], i.e., the actual value of h_0 *does* matter. The second inequality in Eq. (1.1) is required for a two-scale formulation to make sense. In other words, it is assumed that the macroscopic and the microscopic scales of the problem are clearly separated, and hence, a microscopically informed macroscale differential equation may be formulated [7]. However, unlike η, ε is actually allowed to go to zero although this is not necessary. When it occurs, it physically corresponds to roughness with impenetrable gaps and therefore to an effectively smaller local film thickness $h_{\min} < h_0$. Finally, the order of magnitude interval provided for the third parameter is simply an indication [8] that there is a need to consider local roughness effects, which would be negligible for $\zeta \ll 1$, while avoiding contact between the surfaces, which might occur as ζ approaches $\mathcal{O}(1)$.

Combination of the first two parameters in Eq. (1.1) delivers a fourth key dimensionless parameter

$$\gamma = h_0/\lambda = \eta/\varepsilon \tag{1.2}$$

The central role of this parameter in the derivation of the two-scale problem appears to have been first pointed out in Ref. [7] and subsequently given further mathematical treatment in Ref. [9]. These studies, which will constitute the basis of the numerical investigations in this work, begin the homogenization-based multiscale analysis of the interface with the premise that the actual three-dimensional fluid flow is sufficiently accurately described by Stokes equations, an assumption that will be further addressed shortly. Although ε and η are very small, no explicit restriction is placed on their ratio. Consequently, three different *microscopic regimes* are obtained in the process of deriving the two-scale formulation from the original three-dimensional one under the inequalities (1.1):

(1) *Reynolds regime* is where $\gamma \ll 1$, i.e., η decreases much faster than ε. Consequently, one may first decrease η to obtain the classical two-dimensional Reynolds equation in terms of h which governs the fluid mechanics at a *wavy* interface then decrease ε to obtain a macroscopic Reynolds-type equation that is microscopically governed by this classical equation.
(2) *Stokes regime* is where $\gamma = \mathcal{O}(1)$, i.e., η and ε decrease at the same rate. Consequently, the microscopic problem is still governed by the Stokes equations although the general form of the macroscopic Reynolds-type equation is retained.
(3) *Congested regime* is where $\gamma \gg 1$, i.e., ε decreases much faster than η. Because the rapid reduction in ε effectively leads to a globally smooth variation of the film thickness with a locally reduced value $h_{\min}$, the slower reduction of η essentially leads to the classical Reynolds equation, with the important exception that h is replaced by $h_{\min}$.

Therefore, the first two cases require a two-scale formulation, whereas the last one is essentially a single-scale setting and hence straightforward to handle. Overall, the two-scale formulation of the Stokes regime is the most general framework since one can consistently obtain the Reynolds and congested limits of homogenization by, respectively, further decreasing or increasing γ. However, it is also the most demanding framework with respect to computational cost so that, if possible, it is advantageous to make explicit use of the conventions which are induced by the first and the last regimes. As already indicated earlier, it is assumed that there is a single wavelength associated with both surface coordinates, and therefore, that the value of γ applies to both of these directions. In some sense, one may in general have combinations of these scenarios where the flow is congested along one direction but is in either of the two remaining regimes along the other. This highlights another advantage of the Stokes regime, since it is capable of addressing such complications. It is noted that Bayada and Chambat [7] referred to the regime $\gamma \gg 1$ as *high-frequency roughness*. Since it is not only the roughness frequency but also the film thickness that determines the particular regime, in view of the nondimensional parameter γ, the alternative terminology *congested* is employed in the present study.

Scale separation and different regimes are depicted in Fig. 2, where it is assumed that $\{h_0, L, a\}$ are fixed, with $\eta \ll 1$ and $\zeta = \mathcal{O}(0.5)$ satisfied from the outset, and λ is decreased gradually so that ε will also decrease while γ increases. For any given texture geometry, at large values of λ, $\varepsilon \ll 1$ does not hold, and therefore, the texture actually represents global variations in the interface geometry, similar to waviness. Here, a full numerical resolution of the problem across the interface is feasible. Below a sufficiently small λ when ε takes a value $\varepsilon_0 \ll 1$, a full resolution becomes prohibitively expensive in a numerical setting due to a large number of texture features. However, one observes that a representative solution variable such as the pointwise pressure reaches a limit, i.e., scale separation holds, and hence, a two-scale formulation of the problem is now possible. Up to ε_0, realizations of the same periodic texture which only differ by a phase may show different responses (e.g., textures 1*a* and 1*b*). Such differences vanish beyond ε_0 where different textures may display either partially (e.g., textures 1 and 2) or entirely (e.g., textures 2 and 3) different macroscopic responses. It should be emphasized that scale separation is governed by ε and not γ. However, the value of γ at $\varepsilon = \varepsilon_0$, denoted by γ_0, is almost certainly smaller than 0.1 and lies within the Reynolds regime. As γ further increases with decreasing λ, scale separation continues to hold but eventually a transition between microscopic regimes will occur, first to the Stokes regime at roughly $\gamma = 0.1$ and subsequently to the congested regime at roughly $\gamma = 10$. The macroscopic pressure will increase in a typical wedge problem toward the congested regime since this limit is represented by an effectively homogeneous one at the local minimum film thickness. Although this discussion is qualitative, representative quantitative results which support it may be found in Sec. 3.

The important role of γ has been explicitly recognized very early, apparently first in Ref. [10], where the terms *Reynolds roughness* and *Stokes roughness* have been coined to refer to the

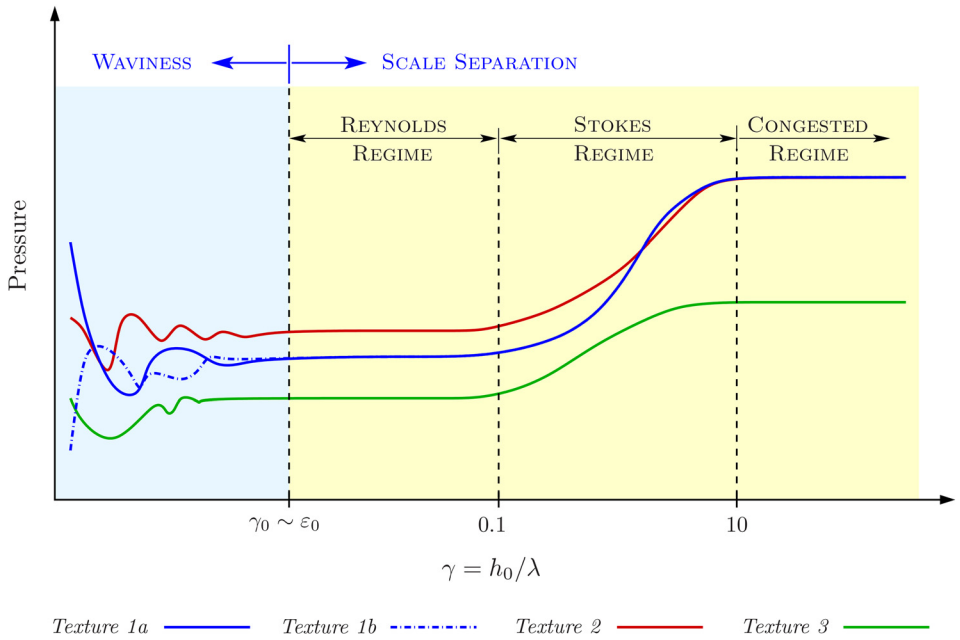

Fig. 2 Scale separation and different regimes are depicted qualitatively for three different textures. Cases 1a and 1b are two realizations of the same periodic texture which only differ by a phase. Here, it is assumed that $\{h_0, L, a\}$ are fixed and only λ is varied. The variation of the pressure with λ may depend on the particular problem. The depicted variation is not based on the numerical results but, where scale separation holds, is only qualitatively associated with the classical wedge problem in a one-dimensional setting with zero Dirichlet boundary conditions and a periodic texture.

two-scale formulations. Therein, the Stokes equations were identified with $\gamma \gg 1$, and hence no reference was made to a congested regime. Moreover, this and the overwhelming proportion of studies on multiscale lubrication studies have concentrated solely on the Reynolds regime. In a limited number of studies, a computational fluid dynamics (CFD) study was carried out at the microscale. However, to the best of our knowledge, despite the rigorous approach of Refs. [7] and [9] and the implications of their analysis, a numerical implementation of their Stokes regime homogenization framework has not been carried out in the literature. Consequently, an investigation of how this framework connects with the Reynolds/congested limit, an identification of major variables which influence this transition between the three microscopic regimes within this particular homogenization approach, and, therefore, a basis for possibly tailoring this transition by varying the texture are missing in the literature. The present contribution aims to fill precisely this gap and will additionally propose an approach for establishing a relation between the three microscopic regimes for complex re-entrant textures where, specifically, the evaluation of the Reynolds limit is not well-defined without further approximation.

1.3 Reynolds Regime. Earliest attempts at incorporating roughness effects have been in the Reynolds regime where both the macroscopic and the microscopic problems are governed by two-dimensional equations—see Refs. [10–13] among others. The pioneering statistical averaging studies in Refs. [8] and [14] proposed a form of the macroscopic Reynolds-type equation which, however, was restricted to an isotropic response or a specific class of anisotropic responses. This restriction was subsequently removed in Refs. [15] and [16] by replacing the scalar constitutive coefficients (*flow factors* [8]) in the Reynolds-type equation with tensorial ones, thereby establishing the final structural form which can represent microscopic roughness effects such as anisotropy on the macroscale. In order to highlight the nonscalar nature of these quantities in the general anisotropic setting, Elrod [15] employed the terminology *flow-coefficient dyads*, whereas Tripp [16] employed *flow factor tensors*, which is the one that will be preferred in the present study. A more recent derivation of this generalization is provided in Ref. [17]. All of these works address random roughness. In particular, Refs. [8] and [14–17] assign roughness and motion to both of the interacting surfaces. Moreover, starting with Ref. [10], the approaches in Refs. [13,15,16] employ some type of an asymptotic expansion combined with averaging in order to arrive at the macroscopic equation. As such, these works constitute precursors to more recent homogenization studies where the two-scale structure of the interface problem is clearly exposed—see Ref. [7] for an early example, where each surface is either rough or moving (*unilateral setting*) and [18] for an extension to the case where roughness and motion are assigned to both surfaces (*bilateral setting*). Although homogenization explicitly invokes a periodic film thickness within the derivation of the two-scale problem, the form of the macroscopic Reynolds-type equation is structurally essentially the same as those obtained from statistical averaging, and the approaches to the determination of the flow factor tensors are also mechanically equivalent. Hence, one may employ random microstructures within the two-scale setting of homogenization as well [19] without any loss of accuracy with respect to the predictive capability of statistical averaging results. However, the loss of accuracy in the overall predictive capability of these two-scale approaches with respect to the deterministic solution of the problem based on a full resolution of random roughness across the whole interface remains an open question. By comparison, the answer to this question in the case of periodicity is rigorously addressed in the context of homogenization.

In the present work, either texture or motion will be assigned to each surface. Moreover, only periodic textures will be considered. CFD studies of lubrication to be reviewed below commonly invoke these assumptions as well, exceptions to which will be noted. Consequently, the unilateral setting of Bayada and Chambat [7] applies in both Reynolds and Stokes regimes. An attempt

to generalize homogenization in the Stokes regime toward the bilateral setting based on Ref. [7], the Reynolds limit of which would be [18], has recently been presented in Refs. [20] and [21].

1.4 Stokes Regime. Roughness influence has a long history in fluid mechanics. Among recent studies, those concerning the formulation of appropriate effective boundary conditions associated with flows over periodic textures [22,23] are particularly relevant, specifically with respect to the multiscale structure of the problem. Presently, the aim is to provide a fairly comprehensive chronological review of microscopic CFD studies which attempt to characterize the macroscopic response of the interface quantitatively, e.g., in terms of quantities which appear in the macroscopic Reynolds-type equation, or qualitatively, e.g., in comparison to the Reynolds limit. Some closely related CFD studies will additionally be mentioned even if they do not directly concentrate on implications for a two-scale analysis. Most studies are two-dimensional and assume incompressibility, unless otherwise noted, which are assumptions that are also invoked in the present study. They often simultaneously address micro-inertia effects as well, mostly only through the incorporation of the convective part of the acceleration term and without an attempt to resolve turbulence. The investigation of micro-inertia effects in hydrodynamic lubrication are outside the scope of the present study—see Ref. [24] for an early study with an experimental focus.

1.4.1 Early Studies. The necessity of considering an explicit microscopic CFD study depending on the value of $\gamma = h_o/\lambda$ from Eq. (1.2) was first highlighted by Elrod [10]. The earliest published CFD study appears to be in Ref. [25], where the Stokes regime was addressed explicitly but only in a deterministic setting on a model lubrication problem with random roughness and without an exact resolution of the flow. However, in a report from the same year, Elrod carried out a comparison of Reynolds and Stokes regimes [26]. This study was closely followed much later by Mitsuya and Fukui [27], by additionally addressing compressibility, on a sinusoidal periodic texture. After Ref. [26], this was the second study where the Reynolds limit was clearly demonstrated by monitoring the load bearing capacity of the interface while varying the periodic texture wavelength λ. Their results, which were compared with those in Ref. [26], indicated that the Stokes regime starts above a value of $\gamma = 0.1$, although the limit toward the congested regime was not addressed.

1.4.2 Conventional Textures. Due to the challenges in the deterministic resolution of the flow for complex interfaces, attention was shifted to a limited number of unit-cells from a sinusoidal texture in a subsequent numerical and experimental study by Hu and Leutheusser [28] based on the finite element method, but with a sole focus on micro-inertia. Similarly, in Ref. [29], the flow within a unit-cell from a sawtooth texture was analyzed by solving Navier–Stokes equations with a collocation method, however, with only a minor emphasis on the influence of texture dimensions. The suitability of Stokes equations for CFD studies within a texture unit-cell was studied in Ref. [30] based on two-dimensional sinusoidal and sawtooth textures as well as on three-dimensional cubic and cylindrical ones. Here, the monitored quantity was the pressure within the unit-cell, and the discussion was centered on the lift-generating effect of inertia at high flow velocities and not on a homogenized response. The study of Song et al. [31] also did not concentrate on the homogenization response but rather on the differences between the pressure distributions, within a unit-cell of periodicity from a sinusoidal texture, obtained from the Navier–Stokes equations through a stream function formulation and from the Reynolds equation.

The comprehensive work of van Odyck and Venner [32] is the third study after Refs. [26] and [27] with an explicit focus on the transition between the Stokes regime and the Reynolds limit, but also without an explicit consideration of the congested limit. This work was based on the analysis of a microgeometry with a local sinusoidal feature through a finite volume discretization of three different microscopic equations: Reynolds equation, Stokes equations, and perturbation equations which link the former to the latter. The results indicated that, in agreement with Refs. [7] and [10], γ is the major parameter which controls the transitions between the three microscopic regimes, apart from the particular shape of the transition curve. Also, in close agreement with Ref. [27], a visible transition to the Stokes regime was identified with $\gamma > 0.1$. The observations in the present study will mostly be in agreement with these results.

1.4.3 Micro-Inertia Effects. A number of studies carried out microscopic analyses without a major focus on homogenization limits but rather on micro-inertia, which are mentioned for completeness. In Ref. [33], finite volume analysis was applied to a single ridge geometry to compare CFD predictions with micro-inertia against the Reynolds equation results. This comparison was made by monitoring the pressure field and by including non-Newtonian effects. Sahlin et al. [34] carried out an investigation of the importance of micro-inertia within a unit-cell by comparing the solutions from Stokes and Navier–Stokes equations. The study of Feldman et al. [35] focused on the deviation of Reynolds and CFD solutions in a unit-cell for realistic geometry parameters associated specifically with laser surface texturing and indicated that, even if large differences are observed in the microscopic pressure distribution, the macroscopic load carrying capacities do not differ significantly. Investigations regarding such macroscopic performance metrics will be outside the scope of the present study. Reference [36] is a rare three-dimensional study of a statistically representative interface with bilateral random roughness, which also appears to be one of the first studies where the flow factors in the theory of Patir and Cheng [8] have been computed using the Lattice Boltzmann method which incorporates micro-inertia effects, but without an explicit concern for homogenization limits. A second such study is by de Kraker et al. [37], where three-dimensional computations were also carried out but within a unit-cell of periodicity and with an emphasis on microcavitation and micro-inertia. It was additionally highlighted that the conventional approach of characterizing pressure-gradient and shear effects individually but then reflecting their combined effect to the macroscale through a linear combination will fail due to the nonlinearity associated with micro-inertia. Subsequent detailed studies and comparisons by Dobrica and Fillon [38] in the presence of micro-inertia indicated that other geometrical parameters in addition to γ may be an important factor in the differences between Reynolds equation predictions and those from Navier–Stokes, which was also concluded earlier in Refs. [27] and [32]. In particular, they demonstrated how the shifted choices of the unit-cell may actually influence the results in a periodic setting due to micro-inertia, thereby questioning the validity of some of the earlier findings in the literature. They also investigated the deterministic solution with a partially textured interface, which was then followed in Ref. [39] where the emphasis was on the difference between Stokes and Navier–Stokes solutions, similar to Ref. [34]. Following Refs. [36] and [37], de Kraker et al. [40] explicitly calculated the flow factors of an interface in the presence of micro-inertia based on a unit-cell via Navier–Stokes, and compared their values to those obtained via Stokes and Reynolds equations with a focus on nonlinearity effects which were earlier discussed in Ref. [37]. More recently, Scaraggi [41] has also presented a comparison of calculations based on Stokes and Reynolds equations within a larger study which concentrated on the influence of the geometric parameters of grooved surfaces on the lubrication response in the Reynolds regime.

1.5 Present Contribution. The summarized review demonstrates various gaps in the literature. First, comparisons between the predictions of Stokes and Reynolds equations without any ambiguity due to micro-inertia effects are scarce [26,27,32,40].

Such a comparison is important since a consensus does not appear to have been reached regarding the influence of micro-inertia. Second, when carried out, comparisons of Reynolds equation predictions with CFD results are rarely pursued in terms of flow factor tensors which appear in the macroscopic Reynolds-type equation [36,37]. Rather, metrics of macroscopic performance are presented, such as the load capacity of the interface, leading to uncertainties in the conclusions with respect to the influence of the boundary conditions and the geometry of the macroscopic problem. Third, in the few sample studies when such calculations are carried out, they are based on the averaging of the microscopic fluid flux rather than on the rigorous Stokes regime scale transition theory of Bayada and Chambat [7] which, therefore, remains unexplored in the literature. Finally, only conventional textures are considered in the literature, such as square/triangular/sinusoidal patterns where complex flow features are missing, and a clear local film thickness definition exists throughout the unit-cell for use within a microscopic Reynolds equation in order to compare its predictions with CFD results. In nonconventional re-entrant textures that display a higher-degree of complexity, leading to an ambiguous film thickness definition, an explicit evaluation of the Reynolds limit remains an open question. The present work attempts to address these shortcomings. In addition, various numerical methods have been applied in these studies, ranging from finite element to finite volume and stream function to Lattice Boltzmann formulations. In the Stokes regime where the ratio of the surface area of the unit-cell to its volume is minimal compared to the two neighboring regimes, the boundary element method (BEM) is a particularly appealing numerical approach in terms of efficiency, yet this method has not been employed so far. Therefore, a side goal of the present study is to explore the application of BEM to homogenization studies in lubrication.

Remark. It was brought to our attention that, while our manuscript was still under review, a study with a similar goal as the present study was very recently accepted for publication [42]. Overall, while the two studies share the same major goal, their scopes are not identical but rather complementary in nature, and future readers will benefit from both of them. On the numerical side, the study in Ref. [42] employs a commercially available software package to carry out representative two- and three-dimensional analyses in order to demonstrate the convergence of the Stokes regime predictions to the two limits. In the three-dimensional case, only a single macroscopic quantity, namely A_{11} with the present notation, was computed due to the high cost associated with multiple cell problems in the Stokes regime. In our study, we have developed our own BEM code, which enabled us to rapidly carry out a large number of computations, thereby resulting in a comprehensive picture of the texture geometry influence, albeit in two dimensions. On the analysis side, we have systematically and extensively addressed various geometrical parameters on conventional textures which differ from Ref. [42], and finally, took an additional step towards re-entrant textures. Together, these two studies demonstrate the implications of the theory of Bayada and Chambat [7] for the first time.

2 Two-Scale Formulation

2.1 Microscopic and Macroscopic Scales. In this section, the governing microscopic and macroscopic equations of the two-scale hydrodynamic lubrication problem are outlined within the limitations of the assumptions stated earlier, based on the analysis in Ref. [7]. For brevity, only the final results of the homogenization analysis will be noted. The numerical investigations will be carried out in a reduced-dimensional setting. In this setting, the interface is one-dimensional in the Reynolds regime so that the microscopic problems may be solved analytically. However, in the Stokes regime, the reduced dimension of the interface is two, so that a numerical solution is still necessary. Therefore, the homogenization results are presented for a three-dimensional setup in order to maintain generality (Fig. 3).

On the macroscale, the two-dimensional interface is spanned by the position vector $\boldsymbol{x}$. Within the Reynolds regime, the microscale analysis is associated with a two-dimensional unit-cell $\mathcal{Y}_R$ which is spanned by a position vector $\boldsymbol{y}$. Within the Stokes regime, the unit-cell is three-dimensional and will be denoted by $\mathcal{Y}_S$. The same notation for the position vector will be employed in both regimes with the understanding that the position vector $\boldsymbol{y}$ has only two components in the Reynolds regime and three components in the Stokes regime. Two types of averages of a quantity over $\mathcal{Y}_R$ and $\mathcal{Y}_S$ will be defined

$$\langle\cdot\rangle_R = \frac{1}{|\mathcal{Y}_R|}\int_{\mathcal{Y}_R} \cdot \, \mathrm{d}a, \quad \langle\cdot\rangle_S = \frac{1}{|\mathcal{Y}_R|}\int_{\mathcal{Y}_S} \cdot \, \mathrm{d}v \tag{2.1}$$

The former is a *surface average*, while the second is a *surface-projected average*. The latter definition is based on the observation that $\mathcal{Y}_R$ represents a domain which is obtained by projecting $\mathcal{Y}_S$ onto the plane spanned by the in-plane (y_1 and y_2) coordinates. It should be emphasized that presently $\mathcal{Y}_S$ represents the *physical* geometry of the texture and not its scaled version, the latter being a common convention in homogenization analysis.

When well-defined, the film thickness variation across the interface may be expressed as

$$h(\boldsymbol{x},\boldsymbol{y}) = h_0(\boldsymbol{x}) - h^-(\boldsymbol{y}) \tag{2.2}$$

where h_0 is the macroscopic variation, and h^-represents the height distribution of the texture on the lower surface with zero mean. Hence, on the three-dimensional Stokes geometry of the unit-cell $h_0 = \langle 1\rangle_S$ and on the two-dimensional Reynolds geometry $h_0 = \langle h\rangle_R$. The minimum value of h over a unit-cell will be indicated by $h_{\min}$.

2.2 Macroscopic Problem. The macroscopic interface mechanics is governed by the Reynolds-type equation which is specialized to the unilateral homogenization setting, subject to standard boundary conditions

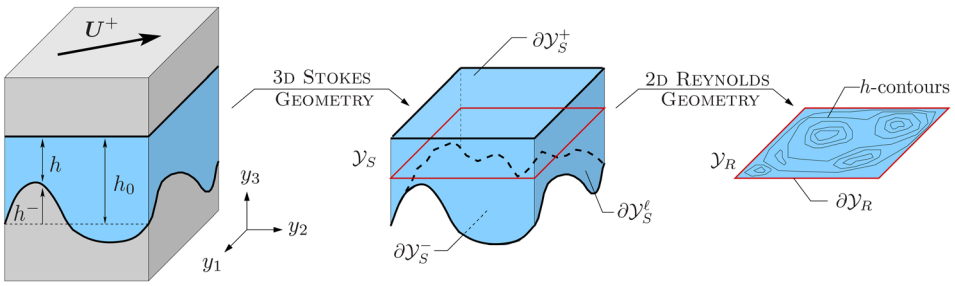

Fig. 3 The physical unit-cell geometry with relevant problem variables, the three-dimensional fluid domain for the solution of the Stokes problem, and its two-dimensional projection onto the in-plane coordinates for the solution of the Reynolds problem are depicted

$$-\nabla_{\boldsymbol{x}} \cdot \left(-\boldsymbol{A}\nabla_{\boldsymbol{x}} p_0 + \boldsymbol{C}\boldsymbol{U}^{+}\right) = \frac{\partial h_0}{\partial t} \tag{2.3}$$

Here, the right-hand side is associated with the normal velocity of the upper surface, $\boldsymbol{U}^{+}$ is the tangential velocity of the smooth upper surface, and $p_0(\boldsymbol{x})$ is the pressure at the interface, which represents the solution to the homogenized problem.

The flow factor tensors $\boldsymbol{A}(\boldsymbol{x})$ and $\boldsymbol{C}(\boldsymbol{x})$ embody all texture influence, and due to a varying $h_0(\boldsymbol{x})$, their values change across the macroscopic interface. The former represents the sensitivity of the interface fluid flux to a macroscopic pressure gradient in a *Poiseuille* problem, whereas the latter represents the sensitivity to boundary motion in a *Couette* problem. For a homogeneous interface (i.e., no texture: $h^{-}=0$), indicating the identity tensor by $\boldsymbol{I}$ and the fluid viscosity by μ, they have the classical forms

$$\boldsymbol{A}_0 = \frac{h_0^3}{12\mu}\boldsymbol{I}, \quad \boldsymbol{C}_0 = \frac{h_0}{2}\boldsymbol{I} \tag{2.4}$$

such that Eq. (2.3) condenses back to the classical Reynolds equation. Otherwise, in general, the solution of a set of microscopic *cell problems* is necessary in order to determine the values for $\boldsymbol{A}$ and $\boldsymbol{C}$. This is numerically challenging in a two-scale setting because at every point across the interface a separate set of cell problems must be solved, due to the dependence of $\{\boldsymbol{A},\boldsymbol{C}\}$ on h_0. These problems are presented in increasing order of complexity. It should be noted that the constant viscosity μ will be retained within the cell problems. An alternative approach would be to filter it out of these problems and directly express its influence within the definition of the flow factor tensors, thereby highlighting the fact that texture influence is geometrical. Indeed, in all regimes, $\boldsymbol{A}$ is inversely proportional to μ, and $\boldsymbol{C}$ is independent from it.

2.3 Microscopic Problems

2.3.1 Congested Regime. In the congested (C) regime, an explicit solution of a microscopic problem is not required. The particular expressions for $\boldsymbol{A}$ and $\boldsymbol{C}$ in this regime have forms which are similar to Eq. (2.4)

$$\boldsymbol{A}_C = \frac{h_{\min}^3}{12\mu}\boldsymbol{I}, \quad \boldsymbol{C}_C = \frac{h_{\min}}{2}\boldsymbol{I} \tag{2.5}$$

2.3.2 Reynolds Regime. In the Reynolds (R) regime, one constructs two decoupled cell problems posed over $\mathcal{Y}_R$

$$\nabla_{\boldsymbol{y}} \cdot \boldsymbol{\varphi} = 0, \quad \nabla_{\boldsymbol{y}} \cdot \boldsymbol{\Phi} = 0 \tag{2.6}$$

where

$$\boldsymbol{\varphi} = \frac{h^3}{12\mu}\boldsymbol{I} + \frac{h^3}{12\mu}\nabla_{\boldsymbol{y}}\boldsymbol{\omega}, \quad \boldsymbol{\Phi} = \frac{h}{2}\boldsymbol{I} + \frac{h^3}{12\mu}\nabla_{\boldsymbol{y}}\boldsymbol{\Omega} \tag{2.7}$$

Using $(\cdot)^{\mathrm{T}}$ to indicate transpose, the particular expressions for $\boldsymbol{A}$ and $\boldsymbol{C}$ in this regime then follow from the solutions of these cell problems for the two-dimensional vectors $\boldsymbol{\omega}$ and $\boldsymbol{\Omega}$, subject to periodic boundary conditions on the boundary $\partial\mathcal{Y}_R$

$$\boldsymbol{A}_R = \langle\boldsymbol{\varphi}\rangle_R^{\mathrm{T}}, \quad \boldsymbol{C}_R = \langle\boldsymbol{\Phi}\rangle_R^{\mathrm{T}} \tag{2.8}$$

2.3.3 Stokes Regime. In the Stokes (S) regime, two sets of decoupled Stokes-type cell problems are solved for $\alpha=\{1,2\}$:

(1) Poiseuille problem: The first set is driven by Poiseuille conditions and governed by

$$\mu\Delta_{\boldsymbol{y}}\boldsymbol{\omega}^{\alpha} = \nabla_{\boldsymbol{y}}\pi^{\alpha} + \boldsymbol{e}^{\alpha} \quad \text{and} \quad \nabla_{\boldsymbol{y}}\cdot\boldsymbol{\omega}^{\alpha} = 0 \quad \text{in} \quad \mathcal{Y}_S \tag{2.9}$$

which are to be solved for the three-dimensional vector $\boldsymbol{\omega}^{\alpha}$ and the scalar π^{α}. These equations are subject to periodic boundary conditions for both variables on the lateral boundary $\partial\mathcal{Y}_S^{\ell}$ as well as $\boldsymbol{\omega}^{\alpha}=0$ on the bottom/top boundary $\partial\mathcal{Y}_S^{-/+}$. It is noted that this problem appears in essentially identical form within the homogenization of two-dimensional porous media [6].

(2) Couette problem: The second set is driven by Couette conditions and governed by

$$\mu\Delta_{\boldsymbol{y}}\boldsymbol{\Omega}^{\alpha} = \nabla_{\boldsymbol{y}}\Pi^{\alpha} \quad \text{and} \quad \nabla_{\boldsymbol{y}}\cdot\boldsymbol{\Omega}^{\alpha} = 0 \quad \text{in} \quad \mathcal{Y}_S \tag{2.10}$$

which are to be solved for the three-dimensional vector $\boldsymbol{\Omega}^{\alpha}$ and the scalar Π^{α}. These equations are subject to periodic boundary conditions for both variables on the lateral boundary $\partial\mathcal{Y}_S^{\ell}$ as well as $\boldsymbol{\Omega}^{\alpha}=0$ on the bottom boundary $\partial\mathcal{Y}_S^{-}$ and $\boldsymbol{\Omega}^{\alpha}=\boldsymbol{e}^{\alpha}$ on the top boundary $\partial\mathcal{Y}_S^{+}$.

In these problems, $\boldsymbol{e}^{\alpha}$ represents unit vectors along the two in-plane coordinates y_{α} of $\mathcal{Y}_S$. Defining two tensors with components

$$\varphi_{\alpha\beta} = \omega_{\beta}^{\alpha}, \quad \Phi_{\alpha\beta} = \Omega_{\beta}^{\alpha} \tag{2.11}$$

the particular expressions for $\boldsymbol{A}$ and $\boldsymbol{C}$ in this regime are

$$\boldsymbol{A}_S = \langle\boldsymbol{\varphi}\rangle_S^{\mathrm{T}}, \quad \boldsymbol{C}_S = \langle\boldsymbol{\Phi}\rangle_S^{\mathrm{T}} \tag{2.12}$$

Note that the presented formulation of the microscopic problems takes one step beyond the presentation of Bayada and Chambat [7] and explicitly delivers the tensor $\boldsymbol{C}_S$. In the original formulation of Bayada and Chambat [7], an effective Couette contribution $\boldsymbol{b}=\boldsymbol{C}_S\boldsymbol{U}^{+}$ to the fluid flux is calculated (see Eq. (2.3)). This is disadvantageous if the problem geometry does not change but only $\boldsymbol{U}^{+}$ changes, because a re-calculation of $\boldsymbol{b}$ would be required every time.

2.4 Conversion Between Volume and Surface Integrals. For the evaluation of $\boldsymbol{A}_S$ and $\boldsymbol{C}_S$, it is advantageous to convert the volume integrals to surface integrals by making use of the divergence-free constraints on the solution fields. Specifically, if $\boldsymbol{v}$ is a vector field such that $\nabla\cdot\boldsymbol{v}=0$ then, denoting the outward unit normal to $\partial\mathcal{Y}_S$ by $\boldsymbol{n}$

$$\int_{\partial\mathcal{Y}_S} \boldsymbol{y}\,(\boldsymbol{v}\cdot\boldsymbol{n})\,\mathrm{d}a = \int_{\mathcal{Y}_S} \nabla\cdot(\boldsymbol{y}\otimes\boldsymbol{v})\,\mathrm{d}v = \int_{\mathcal{Y}_S} \boldsymbol{v}\,\mathrm{d}v \tag{2.13}$$

Upon making use of this expression and observing that $\boldsymbol{\omega}^{\alpha}\cdot\boldsymbol{n}$ and $\boldsymbol{\Omega}^{\alpha}\cdot\boldsymbol{n}$ are nonzero on only $\partial\mathcal{Y}_S^{\ell}$ due to the boundary conditions, one obtains the following expressions as alternatives to Eq. (2.12):

$$\boldsymbol{A}_S = \frac{1}{|\mathcal{Y}_R|}\int_{\partial\mathcal{Y}_S^{\ell}} (\boldsymbol{y}\otimes\boldsymbol{\varphi})\boldsymbol{n}\,\mathrm{d}a, \quad \boldsymbol{C}_S = \frac{1}{|\mathcal{Y}_R|}\int_{\partial\mathcal{Y}_S^{\ell}} (\boldsymbol{y}\otimes\Phi)\boldsymbol{n}\,\mathrm{d}a \tag{2.14}$$

These expressions are particularly convenient in the present study, because only the boundary of the unit-cell is discretized in the context of BEM.

2.5 Scalar Flow Factors. In the Reynolds and Stokes regimes, the macroscopic interface response is possibly anisotropic. Although $\boldsymbol{A}$ is symmetric positive-definite, $\boldsymbol{C}$ is not necessarily symmetric [43] unless the texture response is isotropic. For an isotropic response, the flow factor tensors may be expressed as

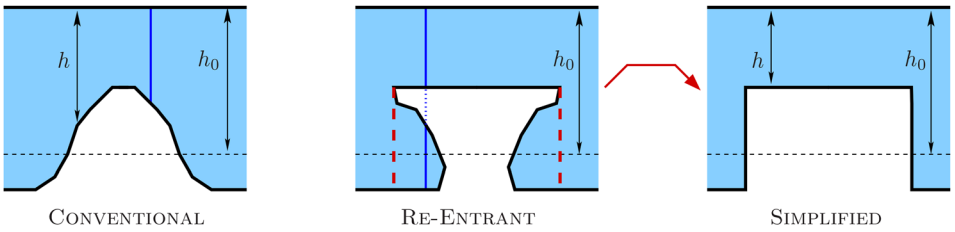

Fig. 4 Conventional/re-entrant texture unit-cells are depicted in two dimensions, and a modification of the original re-entrant texture toward a conventional one with a well-defined film thickness is proposed. In conventional textures, a vertical line (e.g., the solid blue line) across the fluid domain is unbroken by the solid domain, whereas it is broken in re-entrant textures (see color figure version online).

$$\boldsymbol{A} = A\boldsymbol{I}, \quad \boldsymbol{C} = C\boldsymbol{I} \tag{2.15}$$

In the congested regime, the response is necessarily isotropic (see Sec. 1.2) such that it is sufficient to calculate the scalar flow factors A and C, which is also the case for the reduced-dimensional framework of the numerical investigations that is discussed further next.

Remark. In the particular unilateral setting described, it will be numerically observed that both A and C decrease from the Reynolds regime toward the congested regime. This reduction is also monotonic in most cases. Moreover, when compared with the homogeneous interface response (2.4), $A_C \leq A_0$ and $C_C \leq C_0$ clearly also hold. In general, the relative location of A_0 and C_0 with respect to the homogenized response in the Reynolds or Stokes regimes depends on which surface is rough and which one is moving. Nevertheless, as a largely representative guide to the results of the present study, one may state the following ordering relations:

$$A_C < A_S < A_R < A_0, \quad C_C < C_S < C_R < C_0 \tag{2.16}$$

Although these relations are satisfied by almost all of the results in upcoming sections, they are not formal statements, and there may be cases where they are significantly violated.

2.6 Simplifications for Reduced-Dimensional Investigations. The Reynolds regime in a one-dimensional setting leads to analytically solvable cell problems for scalar unknowns $\{\omega, \Omega\}$, delivering the following explicit expressions:

$$A_R = \left\langle \frac{12\mu}{h^3} \right\rangle_R^{-1}, \quad C_R = A_R \left\langle \frac{6\mu}{h^2} \right\rangle_R \tag{2.17}$$

Similar arithmetic- and harmonic-type averages appear within bounds on $\boldsymbol{A}_R$ and $\boldsymbol{C}_R$ [44], closely following similar bounds in the micromechanics of materials [45].

The two-dimensional Stokes regime, with horizontal coordinate y_1 and vertical coordinate y_2, still requires a numerical solution for two-dimensional vectors $\{\boldsymbol{\omega}, \boldsymbol{\Omega}\}$ as well as for the scalars $\{\pi, \Pi\}$, and only a single set of each because the macroscopic reduced-dimension is one. However, the surface integrals (2.14) are now considerably simplified. Decomposing the lateral boundary $\partial\mathcal{Y}_S^\ell$ into periodically linked left/right portions $\partial\mathcal{Y}_S^{\ell,l/r}$, the following expressions hold:

$$A_S = \int_{\partial\mathcal{Y}_S^{\ell,r}} \omega_1 \mathrm{d}y_2, \quad C_S = \int_{\partial\mathcal{Y}_S^{\ell,r}} \Omega_1 \mathrm{d}y_2 \tag{2.18}$$

2.7 Texture Classification and Geometry Simplification. In this work, textures which have a well-defined film thickness in the Reynolds regime are classified as *conventional*, whereas those which do not will be referred to as *re-entrant*. The latter type of textures can display a physically rich behavior in particular when surface tension is present [46–48]. An example is depicted in Fig. 4. For conventional textures that are widely employed in surface engineering, a line through the fluid domain along the y_3-direction is unbroken by the solid domain. For re-entrant textures which have more intricate geometries, however, such a line may be broken. Although this is not a problem in CFD analysis, it renders Reynolds equation inapplicable. Hence, $\{\boldsymbol{A}_S, \boldsymbol{C}_S\}$ can be evaluated but not $\{\boldsymbol{A}_R, \boldsymbol{C}_R\}$.

Within the numerical investigations, re-entrant textures will be modified through geometry simplification in order to obtain a well-defined film thickness (Fig. 4). Subsequently, the limit response obtained from the Stokes regime with increasing texture wavelength λ (or, more properly, decreasing γ) will be compared with an explicit evaluation of the Reynolds limit from the simplified texture geometry. Denoting the flow factor tensors obtained from the simplified texture with $\{\overline{\boldsymbol{A}}, \overline{\boldsymbol{C}}\}$, it is clear that $\{\overline{\boldsymbol{A}}_S, \overline{\boldsymbol{C}}_S\}$ will approach $\{\overline{\boldsymbol{A}}_R, \overline{\boldsymbol{C}}_R\}$ as a limit. The physical motivation, however, is to assess (i) where $\{\boldsymbol{A}_S, \boldsymbol{C}_S\}$ fall with respect to $\{\overline{\boldsymbol{A}}_R, \overline{\boldsymbol{C}}_R\}$ in the Reynolds regime, i.e., to see if the proposed simplification is meaningful, and (ii) where $\{\overline{\boldsymbol{A}}_S, \overline{\boldsymbol{C}}_S\}$ fall with respect to $\{\boldsymbol{A}_S, \boldsymbol{C}_S\}$ in general, i.e., to evaluate the degree to which the re-entrant features of a texture influence its macroscopic response.

It is highlighted, and will be explicitly demonstrated, that the geometry simplification is for analysis purposes only. The *real*

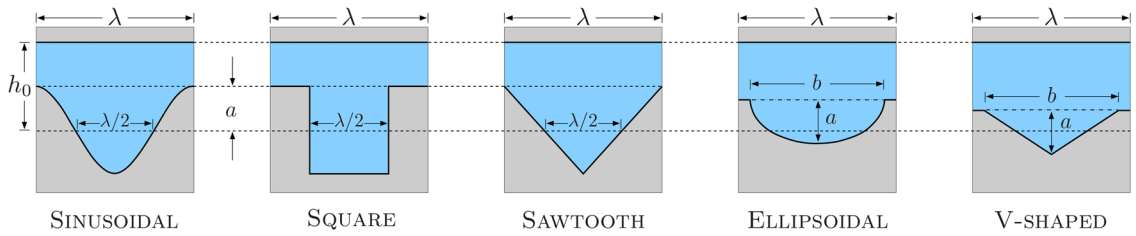

Fig. 5 Unit-cell geometries for conventional textures. For all textures, the only free geometry variables are $\{\lambda, h_0, a\}$. For the ellipsoidal and V-shaped textures, b is adjusted to obtain a desired h_0 once $\{\lambda, a\}$ are specified.

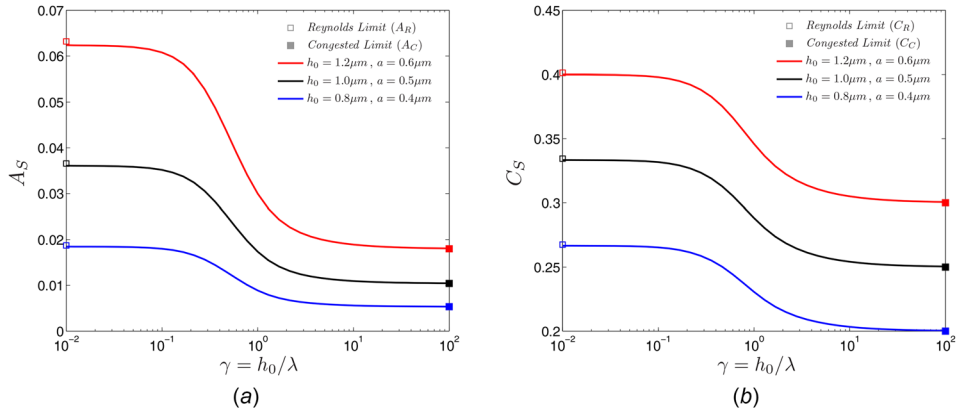

Fig. 6 For the sinusoidal texture with $\lambda = 1$ μm, the variation of $\{A_S, C_S\}$ with γ is shown at different $\{h_0, a\}$ combinations that all share the same value of $\zeta = a/h_0 = 0.5$. Here, and in several subsequent plots, the Reynolds/congested limit is evaluated explicitly and plotted as an empty/filled square with the same color as the corresponding curve: (*a*) A_S variation at different $\{h_0, a\}$ combinations and (*b*) C_S variation at different $\{h_0, a\}$ combinations (see color figure version online).

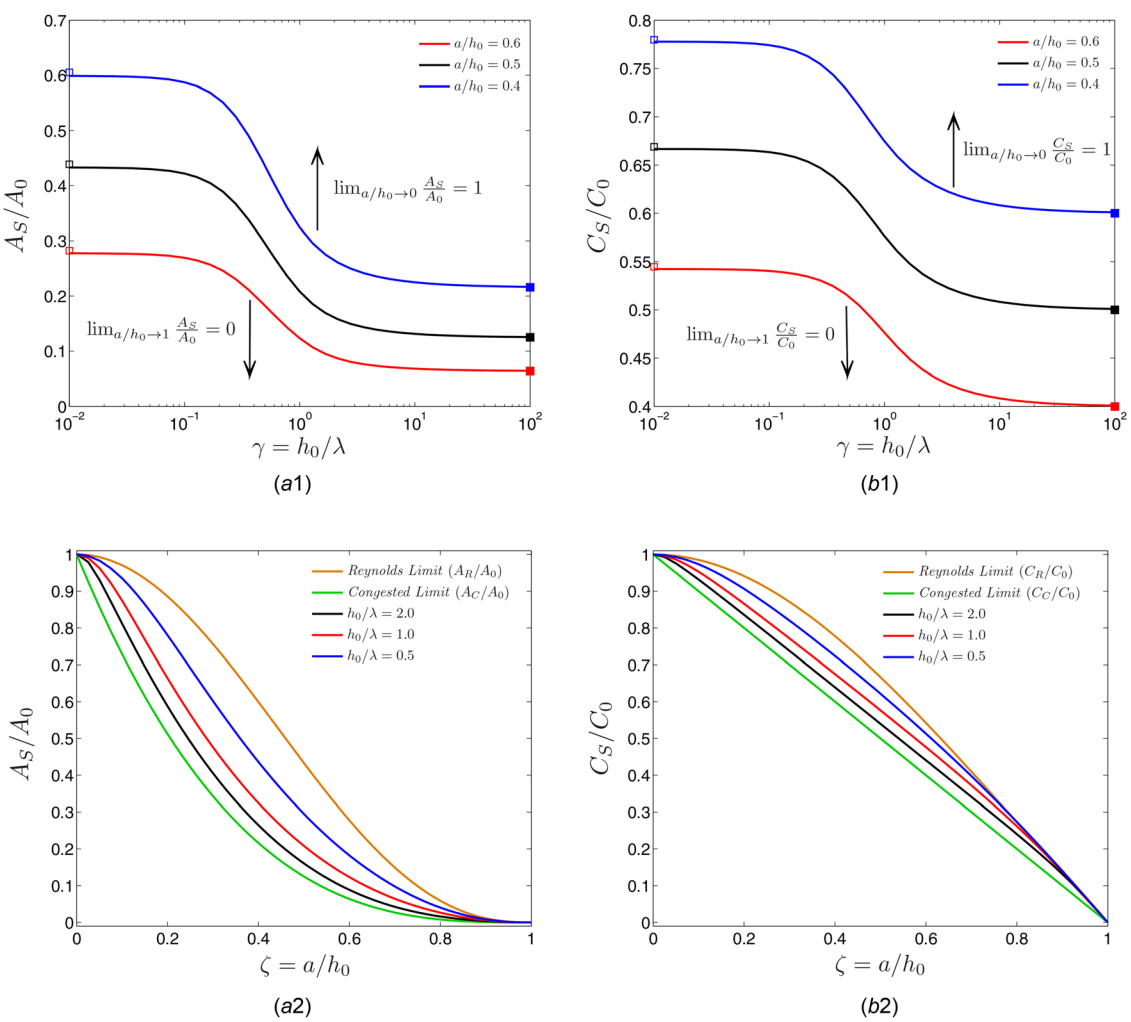

Fig. 7 For the sinusoidal texture, normalization of the homogenized response with the homogeneous one collapses the three curves in Fig. 6 onto the black curves in (*a*-1) and (*b*-1). This normalization will be employed in all subsequent figures. This curve depends on the nondimensional parameter ζ. The boxes indicate the Reynolds and congested limits, as in Fig. 6. The variation of the response with varying ζ at fixed values of γ is shown explicitly in Eqs. (*a*-2) and (*b*-2): (*a*-1) A_S variation at fixed a/h_0 values, (*b*-1) C_S variation at fixed a/h_0 values, (*a*-2) A_S variation at fixed h_0/λ values, and (*b*-2) C_S variation at fixed h_0/λ values.

texture is the re-entrant one, and it is on this texture that $h_0 = \langle 1 \rangle_S = \langle h \rangle_R$ should be satisfied (see Sec. 2.1), not on the *virtual* simplified one. If one attempts to satisfy this mean film thickness relation on the simplified texture by moving the surfaces apart from each other, it will be observed that inferior results will be obtained. The physical reason behind this observation is the fact that fluid is retained within pockets of the re-entrant texture, thereby contributing to the total interface fluid volume, but its motion is restricted such that these pockets effectively act as a part of the texture.

3 Conventional Textures

In the remaining portion of this work, a series of numerical investigations will demonstrate how the macroscopic response of microtextures is influenced by the governing physical parameters of the multiscale problem, starting with conventional geometries and continuing with re-entrant ones, with an emphasis on the transition between the three regimes of lubrication. The solution in the Stokes regime is based on BEM, which is briefly reviewed in Appendix A. The choice of the default numerical discretization and exceptions to this choice are noted in Appendix B. In all investigations, $\mu = 1$ Pa·s is employed without the loss of generality (Sec. 2.2). The solutions to the cell problems (2.9) and (2.10) of the Stokes regime for representative configurations of the textures employed are provided in Appendix C.

The five types of conventional textures employed are shown in Fig. 5. Except for the ellipsoidal and V-shaped textures, the texture geometry is solely controlled by the wavelength λ and the amplitude a. The latter parameter also has a significant influence on the macroscopic response and hence will be varied—see Refs. [49] and [50] among others. Therefore, for a given texture, the macroscopic response is influenced by these geometry variables together with the mean film thickness h_0. As previously emphasized in Sec. 1.5, the macroscopic response will be monitored directly in terms of the flow factors $\{A, C\}$ that are obtained from homogenization, thereby eliminating any effects that are associated with the values of macroscopic local variables such as the pressure gradient $\nabla_x p_0$ or the surface velocity $\boldsymbol{U}^+$ as well as the influence of the particular macroscopic problem setup such as the lubrication interface geometry or the boundary conditions employed in the solution of the macroscopic Reynolds-type equation. The macroscopic response will be monitored directly through the Stokes regime formulation in the majority of examples, since this formulation is capable of capturing the neighboring Reynolds and congested regimes as limit cases.

It is advantageous to demonstrate features of the macroscopic response via nondimensional variables. For the sinusoidal texture, different combinations of $\{h_0, a\}$ at a fixed value of $\lambda = 1$ μm deliver different response curves, as shown in Fig. 6. However, all these combinations share the same value of $\zeta = a/h_0 = 0.5$, which

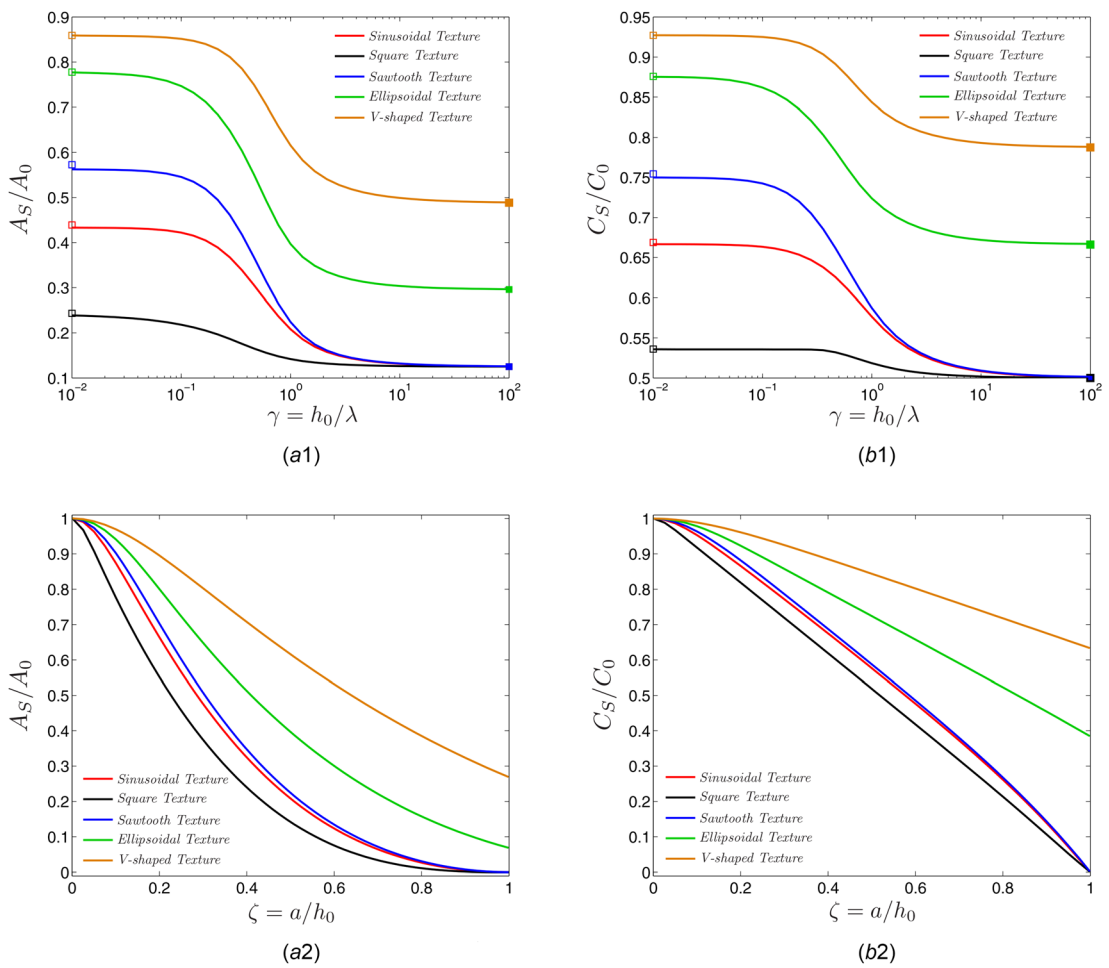

Fig. 8 For different conventional textures, the variation of the macroscopic response with γ at a fixed value of $\zeta = 0.5$ and the variation with ζ at a fixed value of $\gamma = 1$ are shown. The boxes in (*a*-1) and (*b*-1) indicate the Reynolds and congested limits, as in Fig. 6: (*a*-1) A_S variation for conventional textures ($\zeta = 0.5$), (*b*-1) C_S variation for conventional textures ($\zeta = 0.5$), (*a*-2) A_S variation for conventional textures ($\gamma = 1$), and (*b*-2) C_S variation for conventional textures ($\gamma = 1$).

is a major nondimensional variable from Eq. (1.1). To benefit from this observation, $\{A_S, C_S\}$ values can be normalized by representative quantities. Three immediate choice sets are $\{A_0, C_0\}$, $\{A_R, C_R\}$, and $\{A_C, C_C\}$. Presently, the response of the homogeneous interface, i.e., $\{A_0, C_0\}$, will be chosen for normalization, with which all three curves from Fig. 6 collapse onto the same curves in Figs. 7(*a*-1) and 7(*b*-1) for, respectively, A_S and C_S. The limits of these curves are consistent with the Reynolds and congested limits, in agreement with the theoretical predictions. Due to this nondimensionalization, the only remaining control variable is $\zeta = a/h_0$, the variation of which is observed to shift the curve along the vertical direction without a significant change in the range of γ values where the rapid change in the macroscopic response is observed (roughly centered around $\gamma = 1$). Alternative normalization choices would make curves with different ζ values meet at either end: (i) at $\gamma \ll 1$ for normalization with the Reynolds limit where $A_S/A_R \to 1$ and $C_S/C_R \to 1$, and (ii) at $\gamma \gg 1$ for normalization with the congested limit where $A_S/A_C \to 1$ and $C_S/C_C \to 1$. However, it has been observed that the variation of the macroscopic response with ζ at a fixed value of γ is more clearly assessed when the present choice is made. This is demonstrated in Figs. 7(*a*-2) and 7(*b*-2) for different choices of γ, again for the same sinusoidal texture, where the Reynolds and congested limit curves serve as bounding envelopes. The texture influence is diminished as ζ decreases, and the flow is fully obstructed when $\zeta = 1$. Overall, and consistent with earlier observations in the literature as summarized in Sec. 1, neighborhood of $\gamma = \mathcal{O}(1)$ is where the Stokes regime must necessarily be employed. Within one order of magnitude change in γ in either direction, the limiting regimes start to become dominant: below $\gamma = 0.1$, the Reynolds limit is representative of the macroscopic response while above $\gamma = 10$ the congested limit is a good approximation.

With the summarized choices for nondimensionalization, the macroscopic response of different conventional textures with varying γ at fixed ζ as well as with varying ζ at fixed γ are summarized in Fig. 8. Clearly, different textures display different sensitivities to dimensional changes. For instance, the square and sawtooth textures display similar behavior with changing ζ but the sawtooth texture displays stronger variations with γ than the square one. In different applications, different degrees of sensitivity may be desirable from an engineering point of view. Consequently, it is advantageous to work fully in the Stokes regime setting in order to fully benefit from the whole range of macroscopic responses that a texture geometry can deliver, in particular if a new texture is being designed to engineer the macroscopic lubrication response of the interface. Note that as $\zeta \to 1$, the flow in sinusoidal, square, and sawtooth textures become completely obstructed which is reflected by vanishing macroscopic flow factors (Figs. 8(*a*-2) and 8(*b*-2)). The ellipsoidal and V-shaped textures, on the other hand, remain unobstructed due to their geometry description. Again due to the geometry construction, the first three types of textures shared the same congested limit, which differs from the congested limits of the last two textures.

4 Re-Entrant Textures

In this section, the macroscopic response of two types of textures which can display a variable degree of re-entrant features will be investigated (Fig. 9). Specifically, the ratio

$$\xi = b/\lambda \tag{4.1}$$

will control the re-entrant features of trapezoidal and T-shaped geometries, which is a new nondimensional control degree-of-freedom in addition to $\gamma = h_0/\lambda$ and $\zeta = a/h_0$. Both textures are

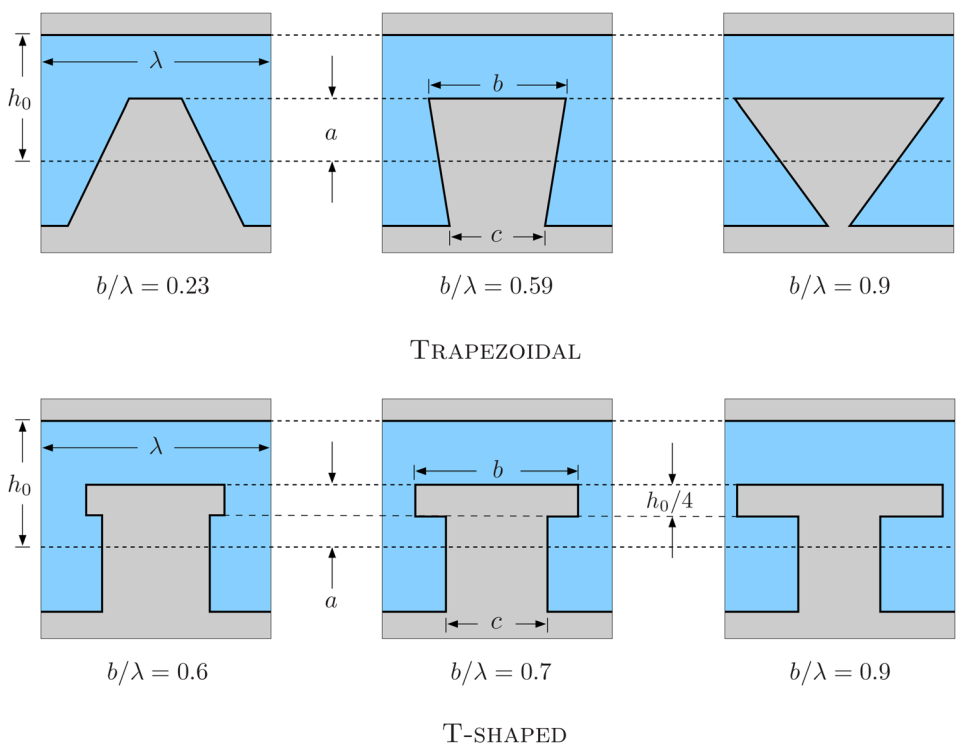

Fig. 9 Unit-cell geometries for two re-entrant textures. The case of $b = c = \lambda/2$ recovers the geometry of the square texture from Fig. 5. With respect to this reference configuration, to control the degree to which the texture is re-entrant, the angle of the vertical surfaces is changed in the trapezoidal surface at fixed values of $\{\lambda, h_0, a\}$ by varying $\{b, c\}$ accordingly. Hence, the trapezoidal texture approaches the sawtooth texture in the limit as $b/\lambda \to 0$. Similarly, for the T-shaped texture, the width of the top portion is changed so that c decreases as b increases. The trapezoidal texture is re-entrant only for $b/\lambda > 0.5$ but the whole range of 0–1 will be tested.

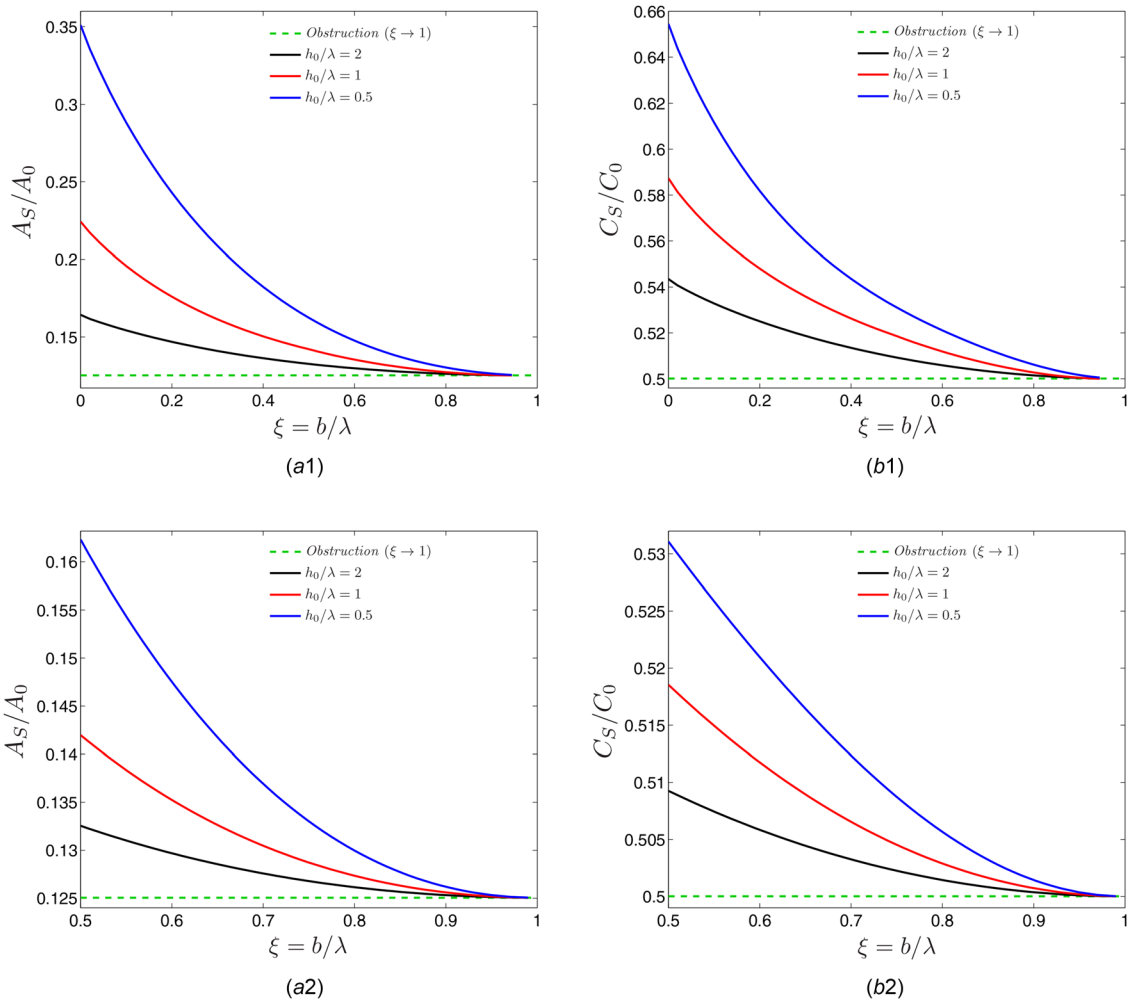

Fig. 10 For the two re-entrant textures, the variation of the macroscopic response with an increasing degree $\xi = b/\lambda$ of re-entrant features is shown at different $\gamma = h_0/\lambda$ values. Despite the value of $\gamma = \mathcal{O}(1)$, $\xi \to 1$ effectively leads to flow obstruction, the limit of which was evaluated explicitly via the congested limit and indicated by the dashed line as a lower bound: (*a*-1) A_S variation for trapezoidal texture, (*b*-1) C_S variation for trapezoidal texture, (*a*-2) A_S variation for T-shaped texture, and (*b*-2) C_S variation for T-shaped texture (see color figure version online).

re-entrant for the range of $\xi \in (0.5, 1)$. The trapezoidal texture retains a conventional geometry in $\xi \in (0, 0.5)$, which will be helpful in the last investigations of this section. In this section, ζ will be fixed at a value of 0.5 since its influence has been demonstrated in Sec. 3. Similarly, the Reynolds and congested limits will not be explicitly indicated on the figures, since the consistency of these limiting formulations with the limit behavior of the Stokes regime formulation has already been verified.

The influence of the control variable ξ is demonstrated in Fig. 10 at different γ values. As expected, at large values of γ the flow is closer to the congested limit and hence is less sensitive to further changes in the geometry. Moreover, increasing ξ has a quantitatively similar effect to ζ since it leads to an increasing obstruction to fluid flow between the re-entrant texture features and thereby to a uniform film thickness that is effectively equivalent to $h_{\min}$. Hence, the limit response as $\xi \to 1$ can be evaluated via the congested limit. The trend in the transition to this limit is identical for both textures.

In order to provide an alternative point of view, as in Fig. 8 for conventional textures, Fig. 11 demonstrates the macroscopic response variation with γ at different values of ξ. Due to flow obstruction, the sensitivity to γ decreases with increasing values of ξ. Although the variations in C_S may be small, in particular for the T-shaped texture, A_S displays significant variations which further highlight the importance of distinguishing between the lubrication regimes.

Despite the comparatively more complicated geometry of re-entrant textures with respect to a square texture, which is recovered at $\xi = 0.5$, it is intriguing to question the importance of fully capturing the re-entrant geometry. For this purpose, the geometry simplification procedure described in Fig. 4 has been applied to re-entrant textures at selected values of ξ. Figure 12 clearly shows that, for both types of re-entrant textures, predictions based on geometry simplification are in excellent agreement with the results from the original re-entrant textures. This is a verification of the previous assertion that the pockets of the re-entrant textures are not domains of active flow so that the fluid in these regions effectively acts as a part of the texture. Note that rapid convergence to the Reynolds limit is also expected for these textures as γ becomes smaller. Presently, a very fine numerical discretization near this limit is required to clearly observe this convergence, as demonstrated in Appendix B. In practice, it would be undesirable to employ very fine resolutions. Thanks to the results to be demonstrated next, it turns out that this is not necessary, because it is possible to switch to the Reynolds equation at small γ values even for re-entrant textures.

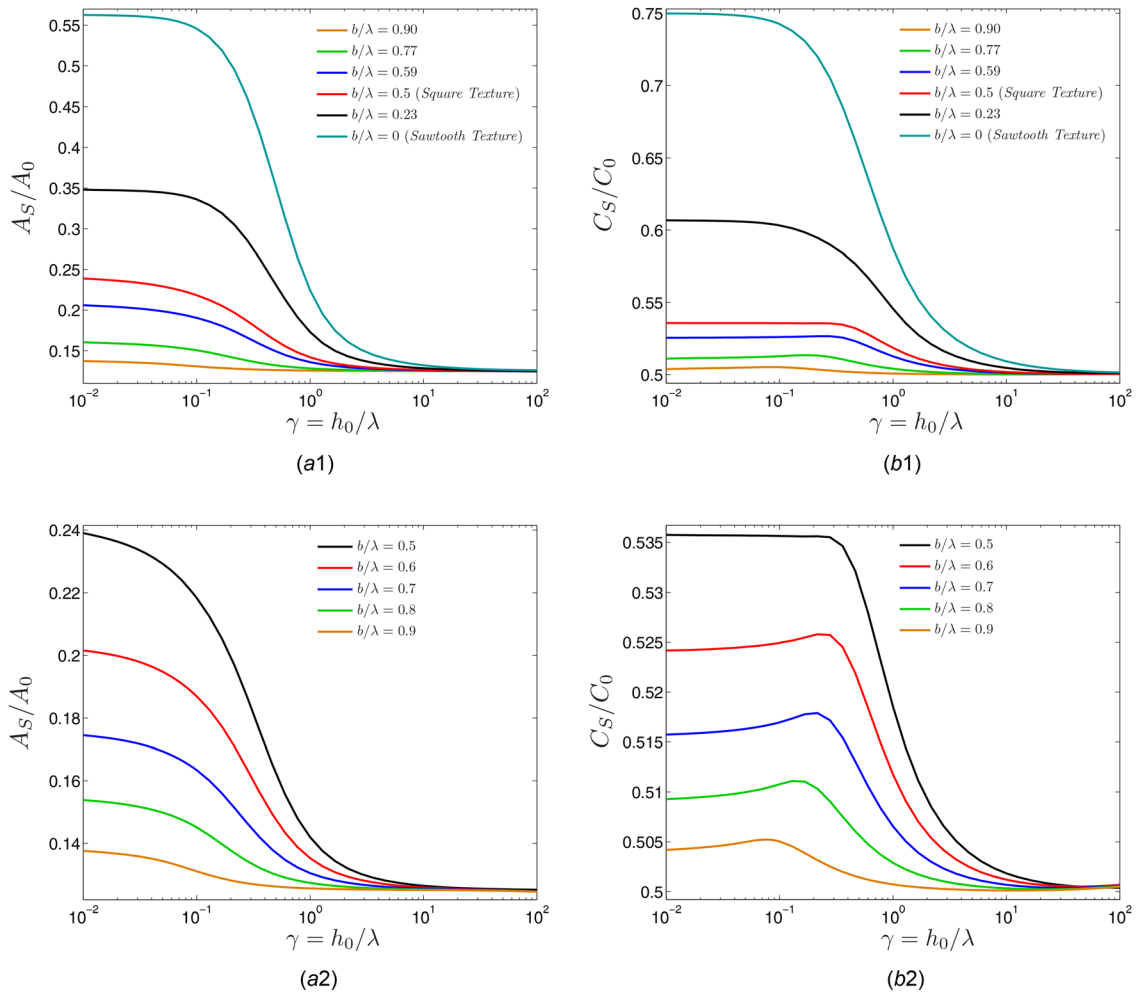

Fig. 11 The variation of the macroscopic response with γ is shown with different degrees $\xi = b/\lambda$ of re-entrant features: (*a*-1) A_S variation for trapezoidal texture, (*b*-1) C_S variation for trapezoidal texture, (*a*-2) A_S variation for T-shaped texture, and (*b*-2) C_S variation for T-shaped texture

The observations of Fig. 12 essentially enable the application of the Reynolds equation to re-entrant geometries where, without geometry simplification, the film thickness would be ill-defined. Such a conclusion would be advantageous since the solution of the Reynolds equation, when applicable, is significantly less costly compared to Stokes equations. This possibility is investigated in Fig. 13. Note that for both types of re-entrant textures, the Stokes regime formulation is applicable at all values of ξ, which forms a reference. For the trapezoidal texture, the values of $\xi < 0.5$ actually lead to conventional geometries where the Reynolds equation is already feasible due to a well-defined film thickness. The good agreement with the Stokes regime formulation shows that the chosen value of $\gamma = 2 \times 10^{-2}$ falls within the Reynolds regime. As ξ is increased beyond 0.5 for the two textures, $\{A_S, C_S\} \approx \{\overline{A}_S, \overline{C}_S\}$ will hold at all values of ξ, i.e., Stokes regime predictions based on the original and the simplified textures are in excellent agreement. This observation was already verified earlier in Fig. 12 for fixed values of ξ and is not explicitly shown in Fig. 13. Moreover, it is now additionally observed that the application of the Reynolds equation to the simplified geometry delivers similar results as well, i.e., $\{A_S, C_S\} \approx \{\overline{A}_R, \overline{C}_R\}$. This good agreement removes the obstacle in the application of the Reynolds equation to re-entrant texture geometries. Finally, as remarked earlier in Sec. 2.7, geometry simplification should *not* be accompanied by a re-adjustment of the distance between the surfaces in order to recover the same value of h_0 when it is calculated on the simplified texture, i.e., as if the texture had a rectangular geometry. Indeed, as demonstrated for the trapezoidal texture, such a re-adjustment leads to a completely wrong trend in the predicted macroscopic response. Here, the Stokes predictions are also displayed to further show that the wrong trend is not due to the use of the Reynolds equation. This result also emphasizes that the good performance of geometry simplification does *not* indicate that re-entrant texture features are not important—they *do* lead to a macroscopic response that significantly differs from a rectangular texture with the same h_0 value, however, this response can be approximated to good accuracy through a proper simplification instead of a full resolution of the geometrical details.

5 Conclusion

Regimes of roughness in lubrication have been an ongoing source of debate in the multiscale mechanics of lubrication interfaces, ever since first attempts to address microscopic effects due to roughness. In particular, the focus of the debate has centered around the suitability of employing the numerically convenient Reynolds equation on the microscopic scale and cases have been identified where computational fluid dynamics analysis has a superior predictive capability with respect to the macroscopic response. This higher predictive capability may have a number of sources, ranging from an ability to capture micro-inertia effects to

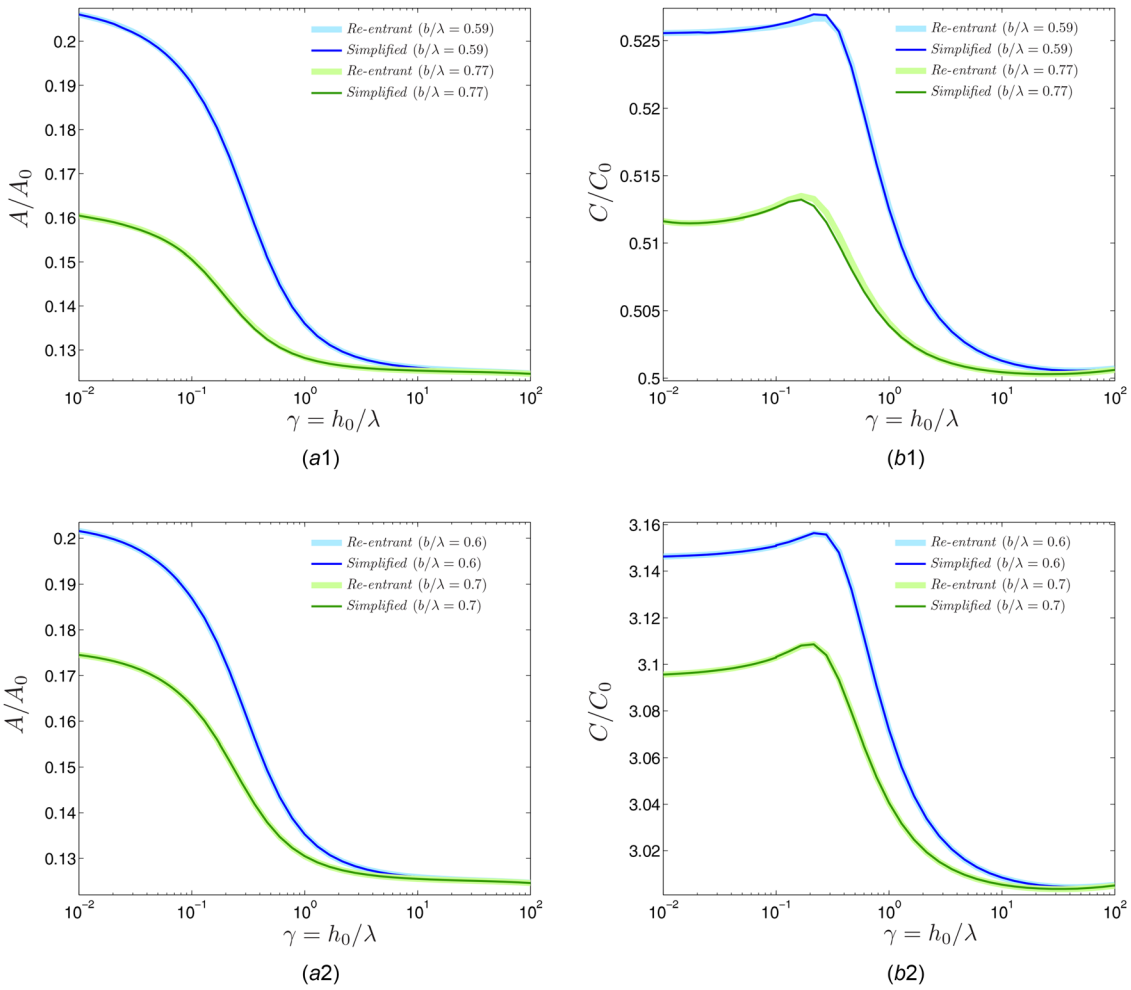

Fig. 12 The macroscopic responses $\{A, C\}=\{A_S, C_S\}$ of the original re-entrant textures and the responses $\{A, C\} = \{\overline{A}_S, \overline{C}_S\}$ of the simplified textures are compared at two different re-entrant configurations (controlled by $\xi = b/\lambda$) from the Reynolds limit to the congested limit based on the formulation of the Stokes regime. The lines toward the Reynolds and congested limits can be further straightened by employing finer mesh discretizations—see Appendix B: (*a*-1) A_S variation for trapezoidal texture, (*b*-1) C_S variation for trapezoidal texture, (*a*-2) A_S variation for T-shaped texture, and (*b*-2) C_S variation for T-shaped texture.

offering a general framework for incorporating complex non-Newtonian fluid behavior. Among such advantages, a fundamental capability is associated with accurately resolving flow characteristics when the texture wavelength is of the order of the film thickness. In this so-called Stokes regime, employing Stokes equations is essentially required. In a pioneering study [7], a two-scale formulation was proposed where Stokes equations were employed on the microscale, and a Reynolds-type equation is employed on the macroscale, together with a rigorous link between the two scales based on homogenization. Moreover, the relation between this formulation and two extreme cases, namely Reynolds and congested limits, was established. The numerical implementation of this theory has been realized for the first time in the present study, based on the numerically efficient boundary element method. Moreover, ambiguities associated with re-entrant textures due to an ill-defined film thickness have been addressed, and an approach to analyzing such complex textures based on geometry simplification has been proposed. Extensive numerical investigations, based on both conventional and re-entrant textures, have clearly demonstrated the link between the three (Reynolds, Stokes, congested) microscopic regimes of hydrodynamic lubrication and how this link depends on the type of the texture. These investigations were carried out strictly based on flow factors which represent the constitutive response of the microtextured interface, thereby eliminating any ambiguities in the conclusions with respect to the macroscopic geometry and the boundary conditions.

A number of studies stand out among various possible future investigations. Among these, a generalization toward a three-dimensional numerical setting is clearly necessary in order to properly assess how the transitions between the three microscopic regimes occur, in particular for anisotropic textures where representative texture wavelengths along each direction may differ. Such an assessment may be carried out not only in terms of flow factor tensors associated with the macroscopic Reynolds-type equation but also in terms of homogenized quantities that characterize frictional heating. In such a setting, it will additionally be possible to design textures which deliver a range of desired macroscopic responses, such as a particular type of anisotropy or a reduced degree of friction, and also assess how the original designs themselves display a geometrical transition through the microscopic regimes. Such investigations will contribute to current widespread efforts in modern surface engineering which aim

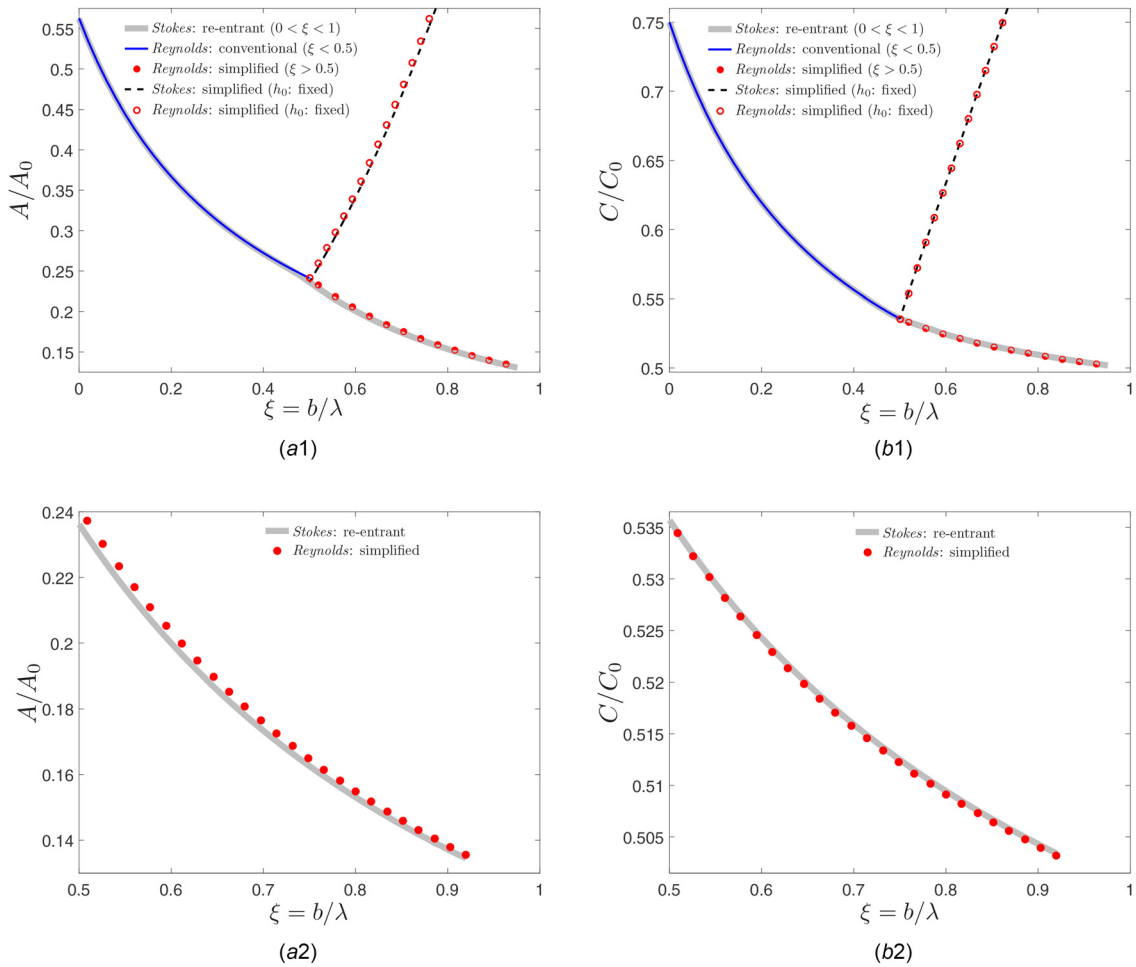

Fig. 13 Near the Reynolds limit ($\gamma = h_0/\lambda = 2 \times 10^{-2}$), macroscopic predictions from different formulations are compared for different degrees $\xi = b/\lambda$ of re-entrant features. For the trapezoidal texture, fixing h_0 corresponds to the adjustment of the gap between the surfaces so as to keep the mean film thickness a constant during geometry simplification which, however, leads to an incorrect trend prediction: (*a*-1) A variation for trapezoidal texture, (*b*-1) C variation for trapezoidal texture, (*a*-2) A variation for T-shaped texture, and (*b*-2) C variation for T-shaped texture.

to simultaneously incorporate multiple and often conflicting demands through complex texture geometries that rely on novel manufacturing techniques.

Funding Data

- The European Commission under the project *MultiscaleFSI* (Grant No. PCIG10-GA-2011-303577).

Appendix A: Boundary Element Method

Boundary element method is a numerical technique which is based on a boundary-only discretization and originates from the integration of the free space Green's function over the elements on the boundaries. If necessary, the solution inside the domain is obtained by postprocessing. In this section, a brief summary of BEM is provided in order to outline the solution of the cell problems in the Stokes regime. For details, the reader is referred to Refs. [51–53].

The governing equations of a steady Stokes flow through a two-dimensional domain $\mathcal{D}$ with position vector $\boldsymbol{x}$ and boundary $\partial\mathcal{D}$, in the absence of an external force, is represented as

$$-\nabla p + \mu\Delta\boldsymbol{u} = 0 \quad \text{and} \quad \nabla\cdot\boldsymbol{u} = 0 \quad \text{in} \quad \mathcal{D} \tag{A1}$$

where p is the pressure, and $\boldsymbol{u}$ is the velocity. When there is a constant external force $\boldsymbol{f}$ per unit volume, p is related to the actual pressure p' via $p = p' - \boldsymbol{f}\cdot\boldsymbol{x}$. As such, both Eqs. (2.9) and (2.10) can readily be associated with the form in Eq. (A1).

Two-dimensional Stokes flow at a point $\boldsymbol{x}_0 \in \mathcal{D}$ admits the boundary integral representation

$$u_j(\mathbf{x}_0) = -\frac{1}{4\pi\mu}\int_{\partial\mathcal{D}} G_{ji}(\mathbf{x}_0,\mathbf{x})\, t_i(\mathbf{x})\mathrm{d}l(\mathbf{x}) + \frac{1}{4\pi}\int_{\partial\mathcal{D}} u_i(\mathbf{x})\, T_{ijk}(\mathbf{x},\mathbf{x}_0)\, n_k(\mathbf{x})\mathrm{d}l(\mathbf{x}) \tag{A2}$$

where $\mathbf{t}$ is the surface traction, $\boldsymbol{G}$ is the velocity Green's function, and $\boldsymbol{T}$ is the stress Green's function. Similarly, the pressure can be expressed through its boundary integral representation

$$p(\mathbf{x}_0) = -\frac{1}{4\pi}\int_{\partial\mathcal{D}} p_j(\mathbf{x}_0,\mathbf{x})\, t_j(\mathbf{x})\mathrm{d}l(\mathbf{x}) + \frac{\mu}{4\pi}\int_{\partial\mathcal{D}} u_i(\mathbf{x})\, P_{ik}(\mathbf{x},\mathbf{x}_0)\, n_k(\mathbf{x})\mathrm{d}l(\mathbf{x}) \tag{A3}$$

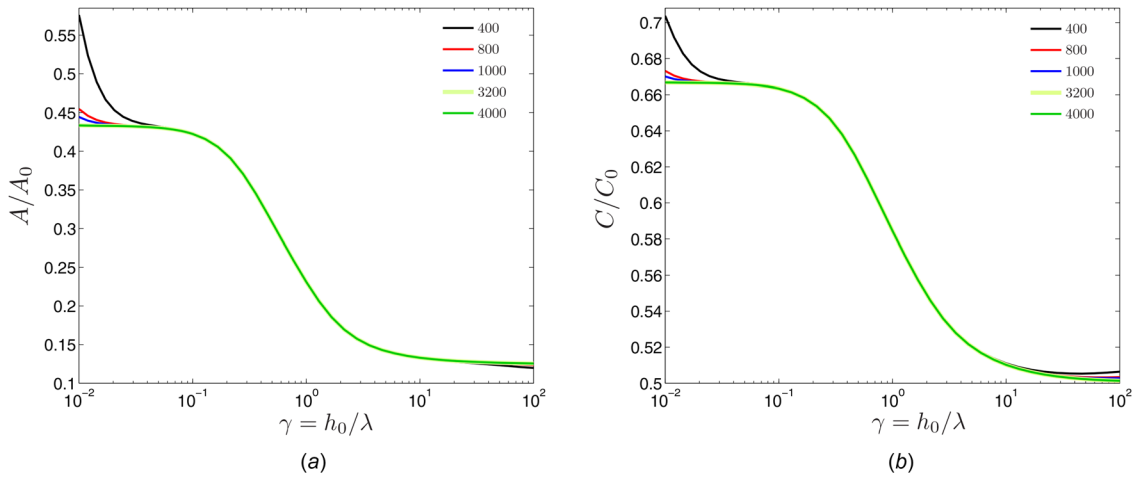

Fig. 14 For the sinusoidal texture configuration with $\zeta = a/h_0 = 0.5$, the influence of regular edge refinement is demonstrated for an increasing total number of elements. The default regular mesh employs 3200 elements: (*a*) A_S variation and (*b*) C_S variation.

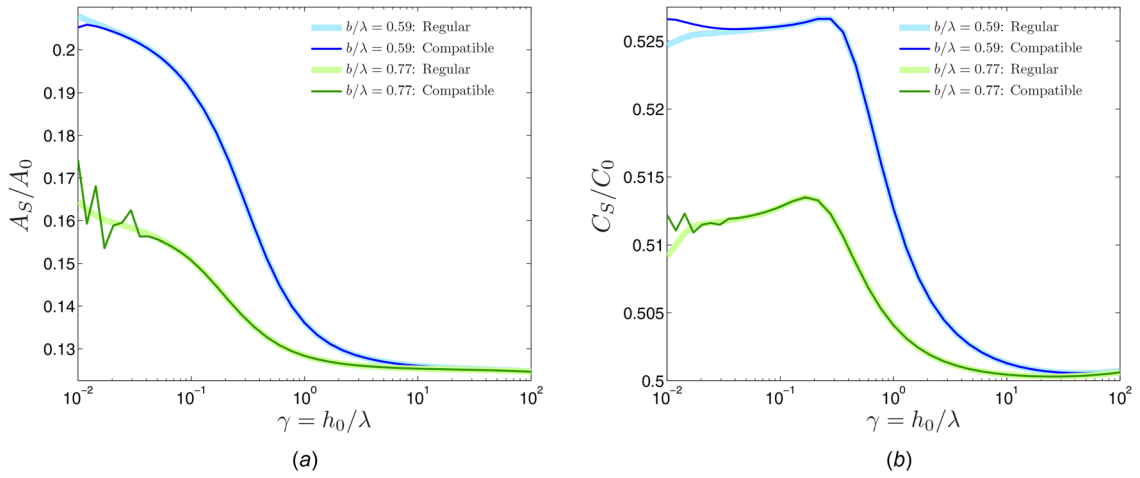

Fig. 15 For re-entrant textures, presently for the trapezoidal texture, switching from a regular to a compatible mesh with the same number of elements (3200) delivers qualitatively better results: (*a*) A_S variation and (*b*) C_S variation

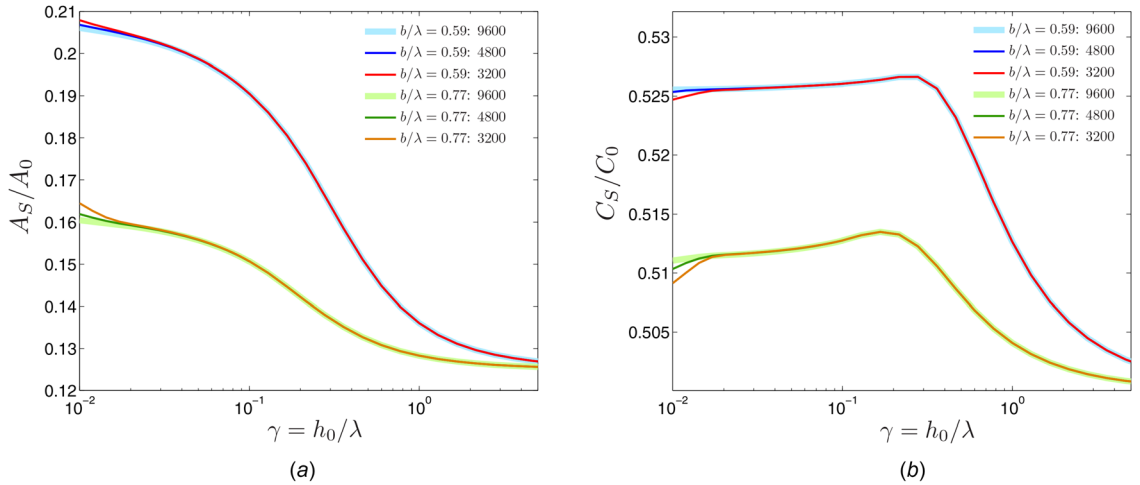

Fig. 16 The compatible mesh results from Fig. 15 are improved by increasing the total number of elements employed from the default value of 3200–9600 in the range $\gamma \in (10^{-2}, 10^{-1})$. The region near the congested limit is excluded to highlight refinement effects more clearly: (*a*) A_S variation and (*b*) C_S variation.

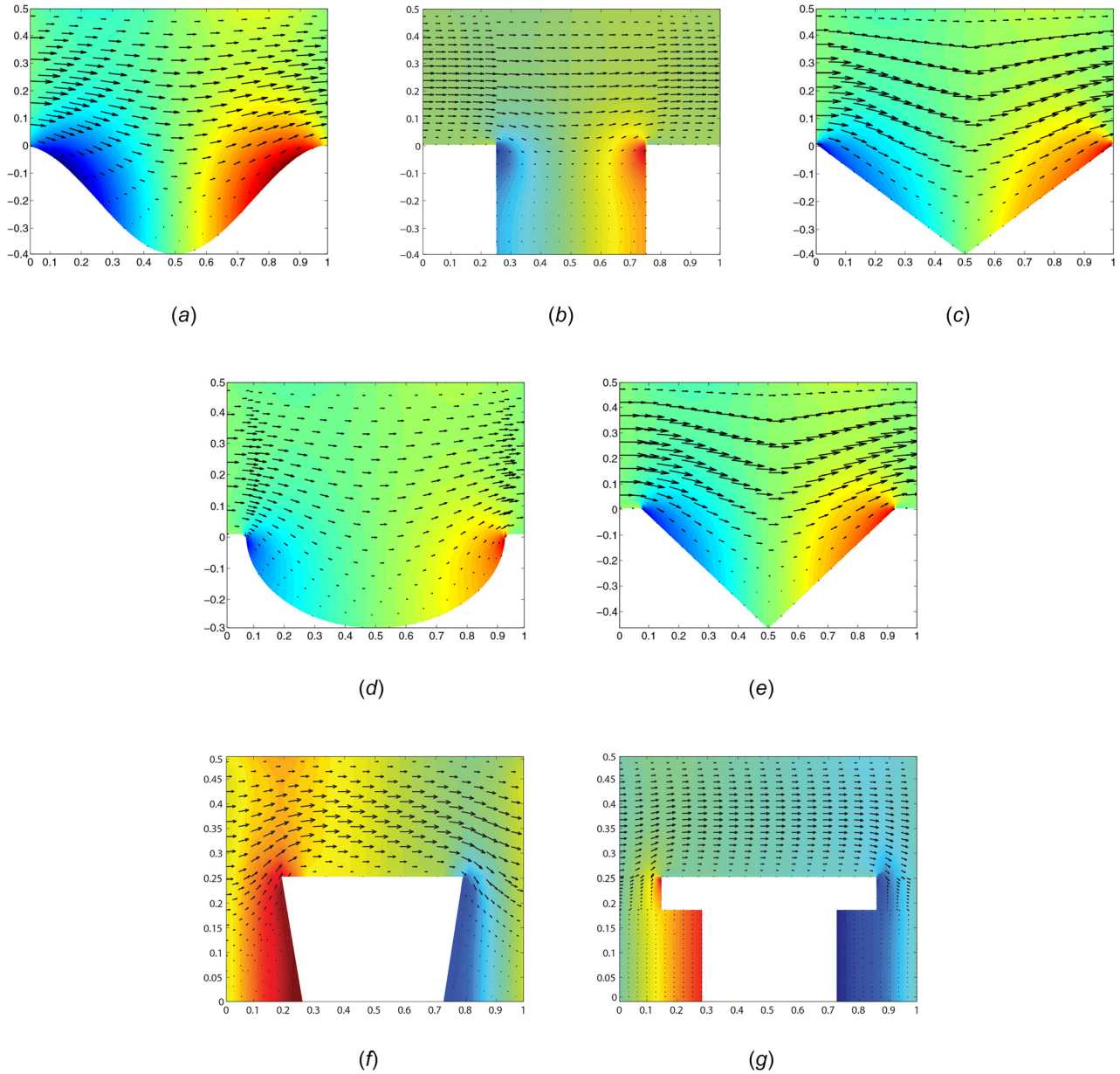

Fig. 17 The solution to the Poiseuille cell problem (2.9) of the Stokes regime is provided for representative texture configurations. The arrows indicate the magnitude and direction of ω while the background color represents π variation (red: high, blue: low) (see color figure version online).

where $\boldsymbol{p}$ and $\boldsymbol{P}$ are pressure terms that are associated with $\boldsymbol{G}$ and $\boldsymbol{T}$, respectively. Defining $\boldsymbol{r} = \mathbf{x} - \mathbf{x}_0$ and $r = |\boldsymbol{r}|$, the Green's functions have the explicit forms

$$G_{ij}(\mathbf{x}, \mathbf{x}_0) = -\delta_{ij} \ln r + \frac{r_i r_j}{r^2}, \quad T_{ijk}(\mathbf{x}, \mathbf{x}_0) = -4\frac{r_i r_j r_k}{r^4} \tag{A4}$$

with the associated terms

$$p_j(\mathbf{x}, \mathbf{x}_0) = 2\frac{r_j}{r^2}, \quad P_{ik}(\mathbf{x}, \mathbf{x}_0) = 4\left(-\frac{\delta_{ik}}{r^2} + 2\frac{r_i r_k}{r^4}\right) \tag{A5}$$

Therefore, once the velocity and traction distributions on $\partial\mathcal{D}$ are known, the complete velocity and pressure fields throughout $\mathcal{D}$ can be obtained using the boundary integral representations (A2) and (A3). The visualizations of the cell problems in Appendix C have been generated based on these expressions.

Now, to solve for the distributions on $\partial\mathcal{D}$, the boundary integral representation (A2) may first be converted into an integral equation by taking the limit as the point $\mathbf{x}_0$ approaches $\partial\mathcal{D}$. After accounting for the singularities in $\boldsymbol{G}$ and $\boldsymbol{T}$, one obtains

$$u_j(\mathbf{x}_0) = -\frac{1}{2\pi\mu}\int_{\partial\mathcal{D}} G_{ji}(\mathbf{x}_0, \mathbf{x})\, t_i(\mathbf{x}) \mathrm{d}l(\mathbf{x}) + \frac{1}{2\pi}\int_{\partial\mathcal{D}} u_i(\mathbf{x})\, T_{ijk}(\mathbf{x}, \mathbf{x}_0)\, n_k(\mathbf{x}) \mathrm{d}l(\mathbf{x}) \tag{A6}$$

The line integrals may then be approximated as the sum of integrals over boundary elements E_n, $n = 1,\ldots, N$. Assuming element-wise constant values u_i^n and t_i^n for the velocity and the traction along x_i-direction on element E_n, the definition of the element integrals

$$\alpha_{ji}^n(\boldsymbol{x}_0) = \frac{1}{2\pi\mu}\int_{E_n} G_{ji}(\mathbf{x}_0, \mathbf{x}) \mathrm{d}l(\mathbf{x}) \tag{A7}$$

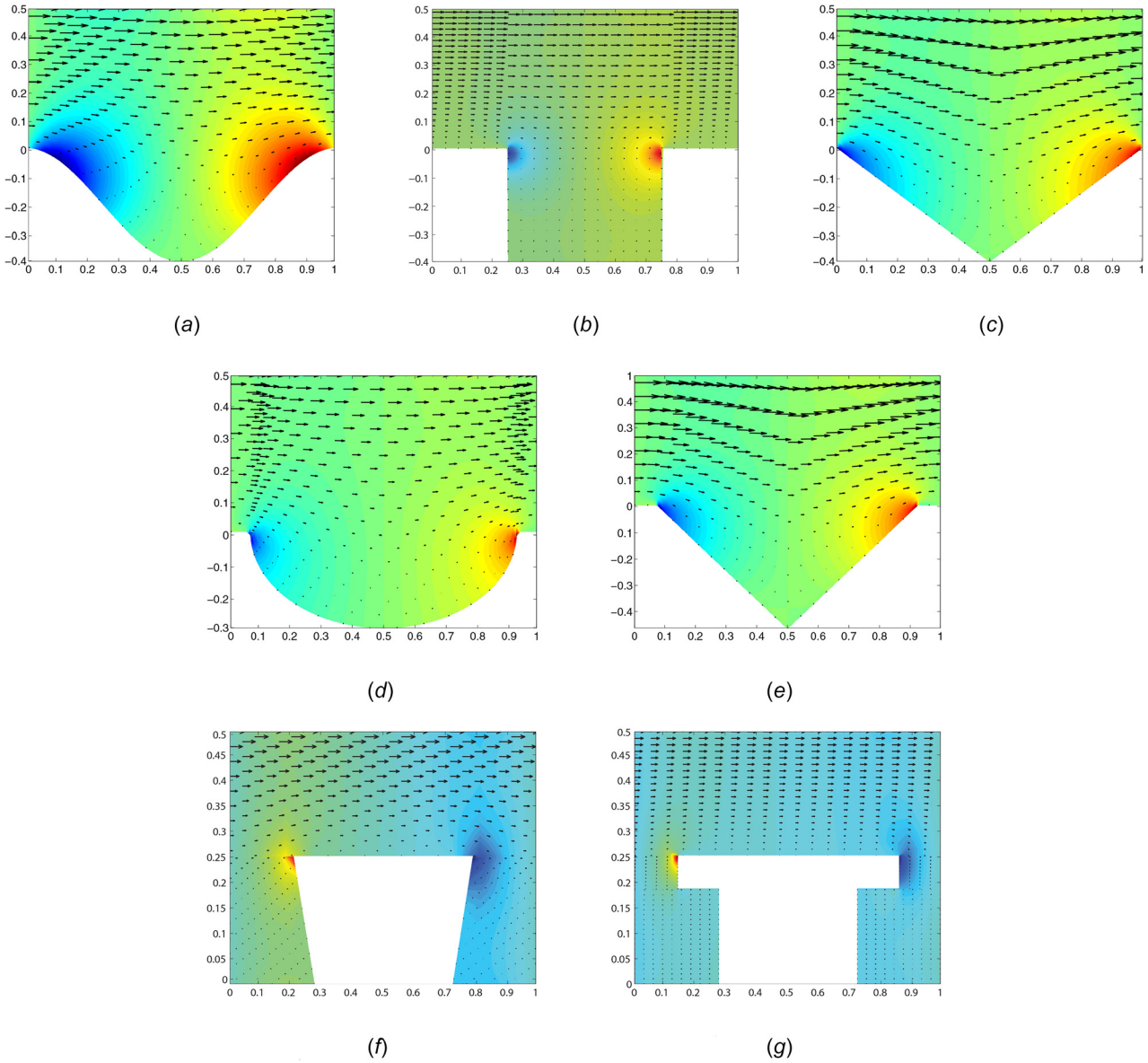

Fig. 18 The solution to the Couette cell problem (2.10) of the Stokes regime is provided for representative texture configurations. The arrows indicate the magnitude and direction of Ω, while the background color represents Π variation (red: high, blue: low) (see color figure version online).

$$\beta_{ij}^{n}(\boldsymbol{x}_0) = \frac{1}{2\pi}\int_{E_n} T_{ijk}(\mathbf{x}_0,\mathbf{x}) n_k(\mathbf{x}) \mathrm{d}l(\mathbf{x}) \tag{A8}$$

leads to the following discretized form of Eq. (A6) for the velocity degree-of-freedom over element E_m with $\boldsymbol{x}_0^m$ as its midpoint:

$$u_j^m = -\sum_{n=1}^{N} \alpha_{ji}^{n}(\boldsymbol{x}_0^m)\, t_i^n + \sum_{n=1}^{N} \beta_{ij}^{n}(\boldsymbol{x}_0^m)\, u_i^n \tag{A9}$$

This result may be expressed as a linear system of equations

$$[B]\{u\} = [C]\{t\} \tag{A10}$$

where $\{u\}$ and $\{t\}$ are vectors of dimension $2N$ which incorporate all the velocity and traction components while $[B]$ and $[C]$ are $2N \times 2N$ matrices. After the imposition of the boundary conditions, the system of equations can be converted into the form

$$[A]\{x\} = \{b\} \tag{A11}$$

where $\{x\}$ is a vector of dimension $2N$ which includes the remaining unknown values of velocity and traction degrees-of-freedom, $[A]$ is a $2N \times 2N$ matrix, and the vector $\{b\}$ contains all the known quantities. The boundary conditions are imposed in a standard manner. Here, it is only noted that periodic boundary conditions on the lateral boundary $\partial\mathcal{Y}_S^{\ell}$ in Eqs. (2.9) and (2.10) require the antiperiodicity of the tractions as well.

Appendix B: Numerical Discretization

For the reproducibility of the presented results, BEM discretization is shortly commented upon in this section. Throughout the numerical investigations, effort has been made to employ the same boundary discretization for different textures and configurations. In general, an efficient and simple discretization is to regularly assign the same number of elements to each edge of

the unit-cell. The optimum number of elements is chosen in order to ensure sufficiently converged results in all cases. However, it has been detected that a well-converged regular discretization for the range $\gamma = h_0/\lambda = \mathcal{O}(0.1 - 10)$ may deliver nonconverged results outside of this range toward the Reynolds and congested limits. In such cases, instead of refining the mesh further, switching to a mesh that is compatible with the aspect ratio of the unit-cell, specifically one that preserves the element length along the whole boundary, was found to be numerically more efficient. On the other hand, such a discretization will lead to a changing number of elements per edge as $\gamma = h_0/\lambda$ is varied, which was found to deliver nonsmooth macroscopic response curves at coarse resolutions. Hence, a regular edge discretization will be employed by default, and a switch to a compatible edge discretization will be made when a deterioration in the solution quality is detected.

Figure 14 demonstrates the higher sensitivity of the solution to the mesh in the Reynolds and congested regimes as the number of elements is changed. Only the sinusoidal texture is provided as an example, other conventional textures display similar behavior. Within the Stokes regime, the solution is efficiently captured even with very coarse boundary meshes. The reason for the sensitivity of the solution to the mesh resolution within the limiting regimes is the very large difference in element lengths along each edge. Even then, a total number of 3200 elements already delivers a well-converged solution that differs by at most 1% from the finest discretization solution and was therefore employed for all conventional textures.

The re-entrant trapezoidal and T-shaped textures were found to be much more sensitive to the mesh resolution, which is demonstrated in Fig. 15. The default mesh that was well-converged for conventional textures is not only delivering nonconverged results, indicated by the continuously varying values toward the two limits instead of straight horizontal lines, but can also lead to oscillations in the curve for certain configurations. Keeping the total element number the same, switching to a compatible mesh eliminates the oscillations, although the results are observed to be still nonconverged near the Reynolds and congested limits. The deficiency near the Reynolds regime is more significant, hence further refinement is pursued only in the range $\gamma \in (10^{-2}, 10^{-1})$, as summarized in Fig. 16. Only the trapezoidal texture is analyzed, and the T-shaped one displays similar behavior. The total number of elements in the compatible mesh is further increased first to 4800 and then further doubled, leading to a solution quality near the Reynolds limit that is comparable to the solution quality near the congested limit. Hence, for re-entrant textures, the default mesh is compatible and has 3200 elements, except near the Reynolds regime where 9600 elements will be employed. Employing even finer meshes near both limits will clearly further straighten the lines which, however, will not be pursued to limit the computational cost in view of the large number of configurations tested.

Appendix C: Representative Cell Problem Solutions

The solutions to the cell problems of the Stokes regime for representative configurations of conventional (Fig. 5) and re-entrant (Fig. 9) textures employed are provided in Fig. 17 for the Poiseuille problem (2.9) and in Fig. 18 for the Couette problem (2.10). Note that these solutions depend only on the geometrical configuration of the unit-cell and not on the values of macroscopic local variables or the particular macroscopic problem setup. Because the provided results are representative only, the magnitudes of the solution variables are not explicitly indicated.

References

[1] Szeri, A. Z., 2011, *Fluid Film Lubrication*, Cambridge University Press, Cambridge, UK.

[2] Hamrock, B., Schmid, S., and Jacobson, B., 2004, *Fundamentals of Fluid Film Lubrication*, CRC Press, Boca Raton, FL.

[3] Temizer, İ., and Stupkiewicz, S., 2016, "Formulation of the Reynolds Equation on a Time-Dependent Lubrication Surface," Proc. R. Soc. A, **472**(2187), p. 20160032.

[4] Sanchez-Palencia, E., 1980, *Non-Homogeneous Media and Vibration Theory*, Springer-Verlag, Berlin.

[5] Bayada, G., and Chambat, M., 1986, "The Transition Between the Stokes Equations and the Reynolds Equation: A Mathematical Proof," Appl. Math. Optim., **14**(1), pp. 73–93.

[6] Hornung, U., ed., 1997, *Homogenization in Porous Media*, Springer-Verlag, New York.

[7] Bayada, G., and Chambat, M., 1988, "New Models in the Theory of the Hydrodynamic Lubrication of Rough Surfaces," ASME J. Tribol., **110**(3), pp. 402–407.

[8] Patir, N., and Cheng, H. S., 1978, "An Average Flow Model for Determining Effects of Three-Dimensional Roughness on Partial Hydrodynamic Lubrication," ASME J. Lubr. Technol., **100**(1), pp. 12–17.

[9] Bayada, G., and Chambat, M., 1989, "Homogenization of the Stokes System in a Thin Film Flow With Rapidly Varying Thickness," Math. Model. Numer. Anal., **23**(2), pp. 205–234.

[10] Elrod, H. G., 1973, "Thin Film Lubrication Theory for Newtonian Fluids With Surface Possessing Striated Roughness or Grooving," ASME J. Lubr. Technol., **95**(4), pp. 484–489.

[11] Christensen, H., and Tonder, K., 1971, "The Hydrodynamic Lubrication of Rough Bearing Surfaces of Finite Width," ASME J. Lubr. Technol., **93**(3), pp. 324–330.

[12] Christensen, H., and Tonder, K., 1973, "The Hydrodynamic Lubrication of Rough Journal Bearings," ASME J. Lubr. Technol., **95**(2), pp. 166–172.

[13] Sun, D.-C., 1978, "On the Effects of Two-Dimensional Reynolds Roughness in Hydrodynamic Lubrication," Proc. R. Soc. London Ser. A, **364**(1716), pp. 89–106.

[14] Patir, N., and Cheng, H. S., 1979, "Application of Average Flow Model to Lubrication Between Rough Sliding Surfaces," ASME J. Lubr. Technol., **101**(2), pp. 220–230.

[15] Elrod, H. G., 1979, "A General Theory for Laminar Lubrication With Reynolds Roughness," ASME J. Lubr. Technol., **101**(1), pp. 8–14.

[16] Tripp, J. H., 1983, "Surface Roughness Effects in Hydrodynamic Lubrication: The Flow Factor Method," ASME J. Lubr. Technol., **105**(3), pp. 458–463.

[17] Prat, M., Plouraboué, F., and Letalleur, N., 2002, "Averaged Reynolds Equation for Flows Between Rough Surfaces in Sliding Motion," Transport Porous Media, **48**(3), pp. 291–313.

[18] Bayada, G., Ciuperca, I., and Jai, M., 2006, "Homogenized Elliptic Equations and Variational Inequalities With Oscillating Parameters. Application to the Study of Thin Flow Behavior With Rough Surfaces," Nonlinear Anal.: Real World Appl., **7**(5), pp. 950–966.

[19] Kabacaoğlu, G., and Temizer, İ., 2015, "Homogenization of Soft Interfaces in Time-Dependent Hydrodynamic Lubrication," Comput. Mech., **56**(3), pp. 421–441.

[20] Chupin, L., and Martin, S., 2010, "Rigorous Derivation of the Thin Film Approximation With Roughness-Induced Correctors," SIAM J. Math. Anal., **44**(4), pp. 3041–3070.

[21] Fabricius, J., Koroleva, Y. O., Tsandzana, A., and Wall, P., 2014, "Asymptotic Behavior of Stokes Flow in a Thin Domain With a Moving Rough Boundary," Proc. R. Soc. London Ser. A, **470**(2167), p. 20130735.

[22] Kamrin, K., Bazant, M. Z., and Stone, H. A., 2010, "Effective Slip Boundary Conditions for Arbitrary Periodic Surfaces: The Surface Mobility Tensor," J. Fluid Mech., **658**, pp. 409–437.

[23] Guo, J., Veran-Tissoires, S., and Quintard, M., 2016, "Effective Surface and Boundary Conditions for Heterogeneous Surfaces With Mixed Boundary Conditions," J. Comput. Phys., **305**, pp. 942–963.

[24] Tichy, J. A., and Chen, S.-H., 1985, "Plane Slider Bearing Load Due to Fluid Inertia—Experiment and Theory," ASME J. Tribol., **107**(1), pp. 32–38.

[25] Sun, D.-C., and Chen, K.-K., 1977, "First Effects of Stokes Roughness on Hydrodynamic Lubrication," ASME J. Lubr. Technol., **99**(1), pp. 2–9.

[26] Elrod, H. G., 1977, "A Review of Theories for the Fluid Dynamic Effects of Roughness on Laminar Lubricating Films," Lubrication Research Laboratory, Columbia University, Technical Report, Report No. 27.

[27] Mitsuya, Y., and Fukui, S., 1986, "Stokes Roughness Effects on Hydrodynamic Lubrication—Part I: Comparison Between Incompressible and Compressible Lubricating Films," ASME J. Tribol., **108**(2), pp. 151–158.

[28] Hu, J., and Leutheusser, H. J., 1997, "Micro-Inertia Effects in Laminar Thin-Film Flow Past a Sinusoidal Boundary," ASME J. Tribol., **119**(1), pp. 211–216.

[29] Mateescu, G., Ribbens, C. J., Watson, L. T., and Wang, C.-Y., 1999, "Effect of a Sawtooth Boundary on Couette Flow," Comput. Fluids, **28**(6), pp. 801–813.

[30] Arghir, M., Roucou, N., Helene, M., and Frene, J., 2003, "Theoretical Analysis of the Incompressible Laminar Flow in a Macro-Roughness Cell," ASME J. Tribol., **125**(2), pp. 309–318.

[31] Song, D. J., Seo, D. K., and Schultz, D. W., 2003, "A Comparison Study Between Navier–Stokes Equations and Reynolds Equation in Lubrication Flow Regime," KSME Int. J., **17**(4), pp. 599–605.

[32] van Odyck, D. E. A., and Venner, C. H., 2003, "Stokes Flow in Thin Films," ASME J. Tribol., **125**(1), pp. 121–134.

[33] Almqvist, T., and Larsson, R., 2004, "Some Remarks on the Validity of Reynolds Equation in the Modeling of Lubricant Film Flows on the Surface Roughness Scale," ASME J. Tribol., **126**(4), pp. 703–709.

[34] Sahlin, F., Glavatskih, S. B., Almqvist, T., and Larsson, R., 2005, "Two-Dimensional CFD-Analysis of Micro-Patterned Surfaces in Hydrodynamic Lubrication," ASME J. Tribol., **127**(1), pp. 96–102.
[35] Feldman, Y., Kligerman, Y., Etsion, I., and Haber, S., 2006, "The Validity of the Reynolds Equation in Modeling Hydrostatic Effects in Gas Lubricated Textured Parallel Surfaces," ASME J. Tribol., **128**(2), pp. 345–350.
[36] Brenner, G., Al-Zoubi, A., Mukinovic, M., Schwarze, H., and Swoboda, S., 2007, "Numerical Simulation of Surface Roughness Effects in Laminar Lubrication Using the Lattice-Boltzmann Method," ASME J. Tribol., **129**(3), pp. 603–610.
[37] de Kraker, A., van Ostayen, R. A. J., van Beek, A., and Rixen, D. J., 2007, "A Multiscale Method Modeling Surface Texture Effects," ASME J. Tribol., **129**(2), pp. 221–230.
[38] Dobrica, M. B., and Fillon, M., 2009, "About the Validity of Reynolds Equation and Inertia Effects in Textured Sliders of Infinite Width," Proc. IMechE Part J: J. Eng. Tribol., **223**(1), pp. 69–78.
[39] Cupillard, S., Glavatskih, S., and Cervantes, M. J., 2010, "Inertia Effects in Textured Hdyrodynamic Contacts," Proc. IMechE Part J: J. Eng. Tribol., **224**(8), pp. 751–756.
[40] de Kraker, A., van Ostayen, R. A. J., and Rixen, D. J., 2010, "Development of a Texture Averaged Reynolds Equation," Tribol. Int., **43**(11), pp. 2100–2109.
[41] Scaraggi, M., 2012, "Textured Surface Hydrodynamic Lubrication: Discussion," Tribol. Lett., **48**(3), pp. 375–391.
[42] Fabricius, J., Tsandzana, A., Perez-Rafols, F., and Wall, P., 2017, "A Comparison of the Roughness Regimes in Hydrodynamic Lubrication," ASME J. Tribol., **139**(5), p. 051702.
[43] Waseem, A., Temizer, İ., Kato, J., and Terada, K., 2016, "Homogenization-Based Design of Surface Textures in Hydrodynamic Lubrication," Int. J. Numer. Methods Eng., **108**(2), pp. 1427–1450.
[44] Almqvist, A., Lukkassen, D., Meidell, A., and Wall, P., 2007, "New Concepts of Homogenization Applied in Rough Surface Hydrodynamic Lubrication," Int. J. Eng. Sci., **45**(1), pp. 139–154.
[45] Torquato, S., 2002, *Random Heterogeneous Materials: Microstructure and Macroscopic Properties*, Springer, Berlin.
[46] Tuteja, A., Choi, W., Mabry, J. M., McKinley, G. H., and Cohen, R. E., 2008, "Robust Omniphobic Surfaces," Proc. Natl. Acad. Sci., **105**(47), pp. 18200–18205.
[47] Tuteja, A., Choi, W., McKinley, G. H., Cohen, R. E., and Rubner, M. F., 2008, "Design Parameters for Superhydrophobicity and Superoleophobicity," MRS Bull., **33**(08), pp. 752–758.
[48] Nosonovsky, M., and Bhushan, B., 2016, "Why Re-Entrant Surface Topography is Needed for Robust Oleophobicity," Philos. Trans. R. Soc. A, **374**(2073), p. 20160185.
[49] Bresch, D., Choquet, C., Chupin, L., Colin, T., and Gisclon, M., 2010, "Roughness-Induced Effect at Main Order on the Reynolds Approximation," Multiscale Model. Simul., **8**(3), pp. 997–1017.
[50] Stroock, A. D., Dertinger, S. K., Whitesides, G. M., and Ajdari, A., 2002, "Patterning Flows Using Grooved Surfaces," Anal. Chem., **74**(20), pp. 5306–5312.
[51] Wrobel, L. C., 2002, *The Boundary Element Method* (Applications in Thermo-Fluids and Acoustics), Vol. 1, Wiley, Chichester, UK.
[52] Pozrikidis, C., 2002, *A Practical Guide to Boundary Element Methods With the Software Library BEMLIB*, CRC Press, Boca Raton, FL.
[53] Pozrikidis, C., 1992, *Boundary Integral and Singularity Methods for Linearized Viscous Flow*, Cambridge University Press, Cambridge, UK.